ISSN 1990-7931, Russian Journal of Physical Chemistry B, 2024, Vol. 18, No. 4, pp. 1090–1112. © Pleiades Publishing, Ltd., 2024.

ELECTRIC AND MAGNETIC PROPERTIES OF MATERIALS

Interaction of Nano-Boron Nitride Sheets with Electrodes in Lithium Ion Battery for Increasing Voltage and Amperage

M. Monajjemi[a], *, F. Mollaamin[b], S. Shahriari[c], Z. Khalaj[d], H. Sakhaeinia[a], and A. Alihosseini[a]

[a] *Department of Chemical Engineering, Central Tehran Branch, Islamic Azad University, Tehran, Iran*

[b] *Department of Biomedical Engineering, Faculty of Engineering and Architecture, Kastamonu University, Kastamonu, Turkey*

[c] *Department of Chemistry, Central Tehran Branch, Islamic Azad University, Tehran, Iran*

[d] *Department of Physics, Shahr-e-Qods Branch, Islamic Azad University, Tehran, Iran*

**e-mail: maj.monajjemi@iauctb.ac.ir; m_monajjemi@srbiau.ac.ir*

Received December 7, 2023; revised April 4, 2024; accepted April 22, 2024

Abstract—Nano-Boron nitride compounds have displayed a great potential as anode materials for lithium ion batteries (LIBs) due to their unique structural, mechanical, and electrical properties. The measured reversible lithium ion capacities of Graphene/(h-BN)$_2$/Graphene(G/h-BN/G) based anodes are considerably improved compared to the conventional graphite-based anodes. In this study, the boron nitride sheet has been localized inside the graphene as an option to enhance the electrochemical ratio. Additionally, we have found the structure of G/h-BN/G can improve the capacity and electrical transport in C-BN sheets-based LIBs. Therefore, the modification of BN sheet and design of G/h-BN/G structure provide strategies for improving the performance of BN-G-based anodes. G/h-BN/G could also be assembled into free-standing electrodes without any binder or current collector, which will lead to increase specific energy density for the overall battery design. Finally, we fabricated a novel LIBs and tested our method and we found this system in similar condition using G/h-BN/G increases the voltage and amperage in LIBs. For increasing the capacity, voltage, and amperage for LIBs the composite materials play a strong role. Any theoretical studies in electrode materials (anode and cathode) of lithium ion batteries and subsequent experimental testing with the results of theory can help us to fabricate powerful batteries with low cost. Using Graphene/(h-BN)$_2$/Graphene(G/h-BN/G) based anodes with a suitable composite for cathode materials exhibit high voltages and amperages compared with similar conditions of the previous LIBs.

Keywords: boron nitride sheet, lithium ion battery, graphene sheet

DOI: 10.1134/S1990793124700465

1. INTRODUCTION

Structures of graphite and hexagonal nano-boron nitride (h-BN), parent materials for carbon nanotubes and boron nitride nanotubes are quite similar. They are both layered materials composed of layers of hexagonal lattices; graphite has carbon atoms at all lattice points, while h-BN is composed of alternating atoms of boron and nitrogen. In plane lattice constants are 2.46 Å for graphite [1] and 2.50 Å for h-BN [2]. In contrast to graphite, layered BN is transparent and is an insulator. In h-BN, layers are arranged so that boron atoms in one layer are located directly on top of nitrogen atoms in neighboring layers and vice versa and the hexagons lie on top of each other. In graphite, the stacking is slightly different; hexagons are offset and do not lie on top of each other. Interlayer distances are similar: 3.35 Å for graphite [1] and 3.33 Å for h-BN (Fig. 1) [2]. Electronic properties of graphite and h-BN are radically different from each other. Figure 2 shows theoretical calculations [3] for band structures of a single layer of graphite and h-BN. For a single layer of graphite, graphene, two bands cross each other at Fermi energy. Thus, graphene is a semimetal. Unlike graphene (Fig. 1a), for a single layer of h-BN, equivalent bands do not cross each other and a 4.5 eV band gap forms. Experimentally, bulk h-BN has been measured to have a band gap of 5.8 eV [4]. Crystallographic of BN is classified into four polymorphic forms: Hexagonal BN (h-BN) (Fig. 1b); rhombohedral BN (r-BN); cubic BN (c-BN); and wurtzite BN (wBN). BN does not occur in nature.

In 1842, Balmain W.H. [5] obtained BN as a reaction product between molten boric oxide and potassium cyanide under atmospheric pressure. Thereafter, many methods for its synthesis have reported via (1) h-BN and r-BN are formed under ambient pressure (2) c-BN has synthesized from h-BN under high pressure at high temperature (3) w-BN is prepared from h-BN under high pressure at room temperature [6]. With the discovery of highly reversible, low-voltage Li-intercalation carbonaceous materials, Sony realized the commercialization of xC6/$Li_{1-x}CoO_2$ cells in 1991 [7].

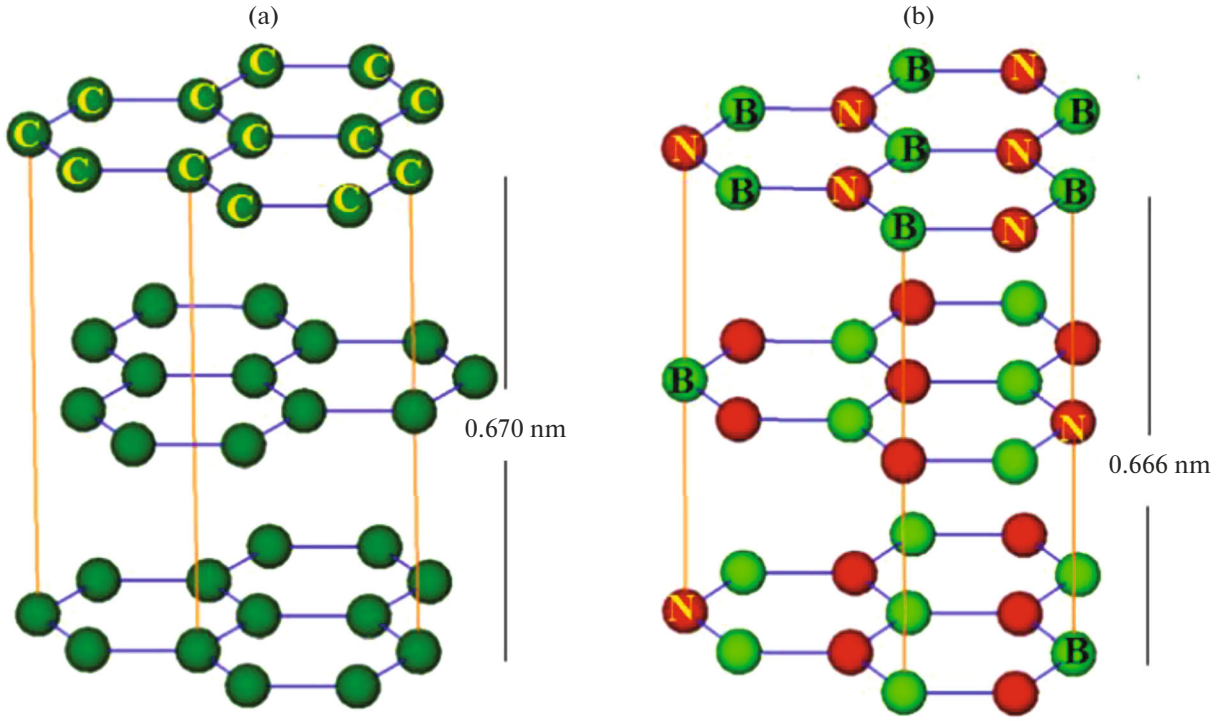

Fig. 1. Crystal structures of (a) graphite; (b) hexagonal boron nitride.

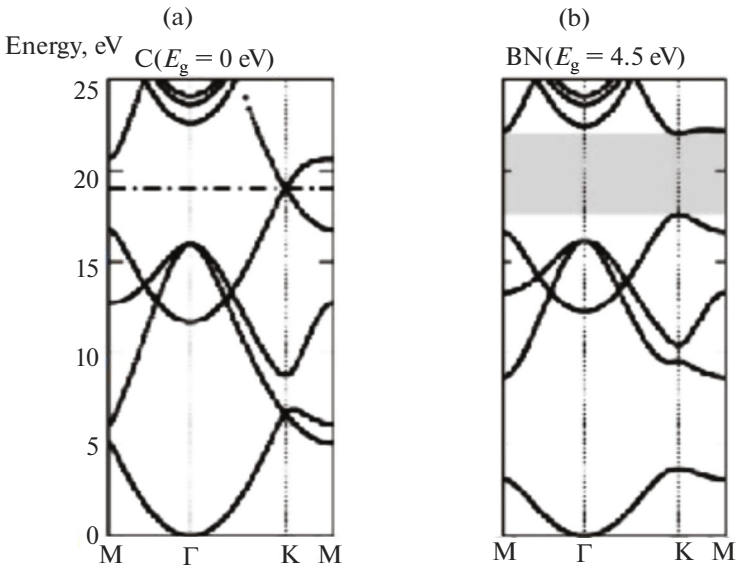

Fig. 2. Comparison of theoretical band structures of a single layer of (a) carbon and (b) h-BN [3].

Lithium ion batteries (LIBs) are representative energy storage devices based on electrochemical energy, widely used in small grid storage systems. The favorable electrochemical performance of LIBs regarding energy and power densities, as well as the progress in cell design and manufacturing, have made LIBs greatly successful for mobile electronics. LIBs typically consist of a positive electrode, a negative electrode, and a conducting electrolyte where store electrical energy in the two electrodes in the form of Li-

intercalation compounds. Electrodes, separator, and electrolyte are the main components of the LIB where the anode plays an essential role in the performance of these devices. During charging of the LIBs, lithium ions released from the cathode move through the electrolyte and are inserted into the anode. Upon discharging, lithium ions are extracted from the anode and move back to the cathode. Although the electrolyte establishes high ionic conductivity between two electrodes, the electrolytes are not responsible for the conduction of free electrons and so the electrons complete the half reaction will move through an extra external wire. Graphite is currently the most common material used for the anodes of commercial batteries because of its capability for reversible lithium intercalation in the layered crystals, which represents the maximum theoretical lithium storage capacity, around, 372 mAh/g [8]. Numerous experiments have been performed to confirm the utilization of graphene nano-sheets and nanoribbons to enhance lithium storage capacity and to improve recharge cyclic performance [9–11]. Furthermore, semi-empirical molecular orbital calculations have been used to investigate lithium ion storage states between two graphene sheets [12], as well as some heteroatom-substituted carbon materials [13–16]. There are a few reviews on anode materials [7–17] and many of them focus on both carbon and inorganic materials. Discharging and charging of Li-ions in graphitized carbon is well established and documented up to now [18–21]. It has also been shown how repulsive forces in a mixed stage can result in a pure stage during intercalation [19]. Although attempts have been made to find suitable replacements, currently only carbonaceous materials are used in commercial anodes [22]. Carbonaceous materials' properties largely depend on the starting materials such as carbon precursor and heat treatment [23]. In this study, charging and discharging of Li-ions has investigated in h-BN with the positive electrode reaction as:

$$LiCoO_2 \rightleftarrows Li_{1-x}CoO_2 + xLi + x\bar{e},$$

and the negative electrode reaction as:

$$xB_3N_3 + xLi^+ + x\bar{e} \rightleftarrows xLiB_3N_3,$$

while the whole reaction is:

$$LiCoO_2 + xB_3N_3 \rightleftarrows Li_{1-x}CoO_2 + xLi\ B_3N_3.$$

It has been suggested that lithium atoms are stored via two mechanisms: intercalation and alloying [24].

Recently many works have been investigated to describe the intercalation and diffusion of Li at different sites on CNTs and many studies have been performed to explain the mechanism by which lithium ions are stored in CNTs, including theoretical works [13–24]. Yang Z.-H. et al. [25] proposed a surface mechanism by which the naked surface of CNTs and carbon nanoparticles can store lithium species, through investigation of the electrochemical intercalation of lithium into raw end closed CNTs. They found that both the outside and inside of the nanotubes are susceptible to lithium intercalations and achieved a high Li density.

Since the CNTs examined were end-caped, and no extra treatments were employed, the lithium adsorbed can only be localized at the surface of CNTs. Graphite is known as a zero-band gap semi-metal due to its unique conduction behavior under the influence of electrical fields [26, 27]. Interlayer forces are small (van der Waals force), and the distance between graphene layers is large (3.35 Å) [21] allowing Li-ions to easily diffuse between graphene sheets. Electrical conductivity of the Li-graphene increases with increasing intercalation levels, due to the electron donor nature of the Li. This is the opposite of ionic conduction in which diffusivity decreases due to the insertion of Li-ions. In the case of amorphous carbon, as the disorder increases, electrical conductivity significantly decreases. Amorphous carbon is known to be composed of small carbon sheets [28] and is of interest due to a much higher capacity than graphitized carbon. The Li-ion diffusivity in amorphous carbon is generally much greater than that in graphitized carbon and the diffusion process can vary widely from one type of carbon to another [29–31]. Surface modification of carbon by mild oxidation, deposition of metals, and coating with polymers or other kinds of carbons has been shown to increase cell performance [32]. Boron doped graphite has also been researched as an option to enhance electrochemical ratio. Amorphous carbon is known to be composed of small carbon sheets [28] and is of interest due to a much higher capacity than graphitized carbon. In our previous works the electronic structures of graphite, h-BN and SWCNTs have been researched [33–39]. While first-principles calculations are not applicable for analyzing the electronic structure of amorphous carbon, various models considering hybridization of sp^3 and sp^2 molecular orbitals have been developed to predict electrical conductivities in this material [40–44]. Classically, a short circuit is defined as a circuit element across which the voltage is zero, regardless of the current flowing through it [45]. Consequences include excessive electric current flow, causing circuit damage, overheating, fire or explosion. From a safety point of view, internal or external short circuits of Li-ion batteries [46] are very important because these can cause a sudden increase in heat generation called thermal runaway [47]. Recently, many researchers have focused on CNT-based anodes for LIBs with varying success, depending on the treatments employed. In this study we have provided new approaches of CNTs in LIB anode applications with respect to structural and dropping properties of boron and nitrogen atoms. As one kind of porous carbon materials, carbon nanotubes (CNTs) have been extensively investigated as anode materials for Li-ion batteries due to their mesoporous character, high chemical stability, low resis-

tance, strong mechanical strength, and high activated surfaces [48–65]. In comparison to the theoretical maximum capacity of graphite at 372 mAh/g (LiC), the electrochemical intercalation of lithium with MWNTs and SWNTs has been studied with higher capacities in recent years [54–63]. MWNTs exhibited reversible capacities of 80–640 mAh/g, while the capacity of the SWNTs was 450–600 mAh/g [64–76]. However, the nature of carbon materials restricts their capacity; some scientists fabricate particular microstructures to improve the electrochemical properties of CNTs. For instance, 1D highly aligned CNT arrays were prepared by the chemical-vapor-deposition (CVD) method [74, 75]. Recently, Fisher group fabricated a tube-in-tube structure with Li + intercalation capacity two times higher than that of the template-synthesized CNTs, as the inner tubules provided more electrochemical active sites for intercalation of Li ions [76]. The intercalation of lithium into graphite involves one lithium atom per six carbon atoms, i.e., LiC6, leading to a limited specific capacity of 372 mAh/g and an observed capacity of 280–330 mAh/g, depending on the type of graphite used [77, 78]. Carbon nanotubes (CNTs), an allotrope of graphite, have been reported to show much improved lithium capacity compared to graphite, due to their unique structures and properties. CNTs have been reported to display conductivities as high as 106 and 105 S m^{-1} for single-walled carbon nanotubes (SWCNTs) and multi-walled carbon nanotubes (MWCNTs), respectively, and high tensile strength up to 60 GPa [79–81]. Obviously, the most direct way to improve the capacity of the CNT anodes is to fabricate composite electrodes of CNTs with other materials. In such hybrid systems, the CNTs function as an effective confining buffer of mechanical stress induced by volume changes in charging and discharging reactions, while the other nanomaterials provide a high capacity. The flexibility, porosity, and conductivity of CNT membranes gave scientists an insight on fabricating ''paper electrodes'' [82–86]. SWNTs were used to fabricate free-standing electrode without polymer binder or a metal substrate, but the capacity was unsatisfactory [83]. CNT networks and aligned CNTs/conducting polymer were then exploited for paper electrodes, and the capacity of the latter was 50% higher than that of SWNT paper electrode [86, 87]. In particular, the Cui group developed CNTs/Si film free-standing electrodes with high specific charge storage capacity 2000 mAh/g and good cycling performance [83]. Later, vertically aligned Si/CNT arrays prepared by the Kumta group also had a capacity of 2000 mAh/g [87]. Hybrid paper electrodes exhibit a promising research prospect. It has been suggested that lithium atoms are stored via two mechanisms: intercalation and alloying [88, 89]. They found that both the outside and inside of the nanotubes are susceptible to lithium intercalations and achieved a high Li density. Since the CNTs examined were end-caped, and no extra treatments were employed, the lithium adsorbed can only be localized at the surface of CNTs. Boron nitride nanotube (BNNT), which was first predicted and synthesized by Rubio and Chopra respectively [90–92], has a structural analogy to CNT but, contrary to the CNT being metallic (semiconductor) depending on chirality. BNNTs are can usually be an insulator regardless of their helicity, tube diameters and number of tube walls [91, 92]. Experimental results have shown that small SWNT are usually found inside multi-walled CNTs. [93, 94] there is, therefore, also a strong motivation to study in detail the stability and interaction of small BNNTs inside a larger one (viewpoint of diameters), which makes easier to understand the experimental results. Besides, the study on double-walled BNNTs (DBNNTs) has demonstrated an interesting variation in their electronic properties when compared with those of free-standing component of BNNTs [95]. So, it is also important to see the inter-wall coupling behavior and interaction energies associated with the small BNNTs. In summary, SWBNNTs and h-BN sheets as one kind of classical materials with a mature studied history will play a significant role in the battery market of the near future, but how to combine hybrid materials together to obtain safe, stable, and high-capacity electrodes has always been the radical problem that many researchers are trying to solve.

2. THEORETICAL BACKGROUND

Li-ion cells included, all key phenomena involve conducting charged particles as a primary cell from cathode to anode or vice versa as a secondary cell from anode to cathode. Typical commercially used lithium-ion battery consists of several interconnected electrochemical cells, where each cell is composed of a graphite anode (such as Meso-carbon microbeads), a cathode formed by lithium metal oxide (such as $LiCoO_2$) and electrolyte (such as LiPF6 dissolved in ethylene carbonate/dimethyl carbonate mixture) embedded in a separator felt.

2.1. Diffusion Lithium Ion in Condensed Materials

Diffusion properties of Li-ion cell determine some of the key performance metrics of Li-ion battery cells, including the charge and discharge rate, practical capacity and cycling stability. The governing equation describing the diffusion process is known as Fick's law as:

$$j_i = -D_i \nabla C_i, \tag{1}$$

and

$$\frac{\sigma C_i}{\sigma t} = \nabla (D \nabla C_i), \tag{2}$$

where j_i is ionic flux, mol cm^{-2} s^{-1}, D_i is diffusivity of solute ($i = 1, 2$), cm^2 s^{-1} and C_i is concentration of spe-

cies i, (mol cm^3) [96]. The proportionality factor D is the diffusivity or diffusion coefficient as

$$D_i = \frac{K_B T}{6\pi\mu R_0}, \quad (3)$$

[96, 97]. In condensed materials both liquids and solids, diffusion is governed by random jumps of atoms or ions, leading to position exchange with their neighbors. The kinetics of this process is temperature dependent and follows an Arrhenius type relationship

$$rate \approx \exp\left(-\frac{\Delta G}{k_B T}\right), \quad (4)$$

[98]. In liquids, the temperature dependence of the diffusion is much less than in solids. Note that no successful first-principles calculation has been made, due to insufficient understanding of the liquid structure [96]. Thus, a simple expression derived from Stoke's drag law is frequently used as an alternative for a diffusivity expression in liquids (Eq. 3) [96]. Although the Li-ion is one of the smallest ions, it is still quite big when compared to electrons; the radius of a Li-ion is ten orders of magnitude larger than that of an electron (radius of a Li-ion: 59×10^{-12} m [99]; radius of an electron: 10^{-22} m [100]). Also the motion of Li-ions is strongly impeded by the potential created by the presence of neighboring ions as discussed below. Thus, diffusion can be the rate-determining process compared to electronic conduction in an electrochemical reaction. The van der Waals interaction, expressed as the Lennard–Jones potential, is relatively weak despite showing a longer interaction range. In the case of the graphite anode, a Li-ion can easily diffuse parallel rather than perpendicular to the graphene layers during intercalation. Thus, in order to understand the diffusion of the Li-ion it is important to consider crystal structure as well as the surrounding potential. Bonding situation in cell component of LIBs can be summarized as: (1) graphite of anode (in-plane) "covalence", (2) graphite of anode (inter-plane) "van der Waals Lennard–Jones", (3) cathode (spinel, $LiMn_2O_4$) "ionic" and (4) Liquid electrolyte "Coulomb". Both the Li-ion diffusivity and electrical conductivity of $LiCoO_2$ are superior to those of $LiFePO_4$ and $LiMn_2O_4$, yielding a possible reason that $LiCoO_2$ displays a higher realized percent of theoretical capacity [101] than the other cathode materials.

2.2. Cathode Materials

Three cathode materials, $LiCoO_2$, $LiMn_2O_4$ and $LiFePO_4$, have represented the majority of LIB cathode research. In an extended approach they can be classified as (1) Layered compounds $LiMO_2$ (M = Co, Ni, Mn), (2) Spinel compounds LiM_2O_4 (M = Mn, etc.) (3) Olivine compounds $LiMPO_4$ (M = Fe, Mn, Ni, Co, etc.). When a Li-ion diffuses out of the cathode (ionic conduction) during the charge cycle the valence state of the transition metal ion changes (electronic conduction); the Fe^{2+} ion is oxidized to Fe^{3+}. The reaction in cathode can be written as:

$$LiFePO_4 - xLi^+ - xe^- \rightleftarrows xFePO_4 + (1-x)LiFePO_4$$

and

$$Fe^{2+} - e^- \rightleftarrows Fe^{3+}.$$

Thus, it is important that electrical and ionic conductivities be optimized in cathode materials, since either of these values can dictate the overall cell properties including capacity and cycle life [102]. Efforts to manipulate the ionic and electrical conductivity of $LiFePO_4$ and $LiMn_2O_4$ via doping have not yet been rewarding. To date, only conductive coatings and particle size reduction techniques have resulted in higher conductivity for cathode materials. Diffusion of a Li-ion in a cathode particle is strongly dependent upon the interaction potential between the Li-ion and the host material structure. A simple model for determining the diffusion path of ions in various crystal structures is introduced in [103]. This model describes the diffusion path as the following:

$$W_T = W_C + W_P + W_R, \quad (5)$$

where W_T is the total potential energy, W_C is the Coulombic interaction, W_P is the van der Waals interaction and W_R is the overlap repulsion between closed shell ions.

2.3. Anode Materials

In the case of anode, Li metal is found to be the most electropositive (−3.04 V versus standard hydrogen electrode) with large reversible capacity (≈4000 A h kg^{-1}). However, due to safety considerations (explosion hazards as a result of dendrite growth during cycling), metallic Li has been substituted by various carbonaceous materials [104]. Carbon-lithium anodes have much lower gravimetric and volumetric energy densities than pure lithium which lead towards the development of interstitial-free 3d transition metal oxides (M nOm, M = Fe, Co, Ni, Mn, Cu). These materials can incorporate more than one Li^+ per metal through conversion (displacement) reactions giving higher capacities (≈800 A h kg^{-1}) in comparison to carbon anodes [105–108]. Conduction in graphite anodes is complex due to continuous phase transformations and the formation of the SEI layer. Phase transformations are reflected in the open-circuit voltage (OCV) curve as distinct plateaus [109]. Also, conduction is strongly dependent upon the degree of crystallinity. As the fraction (f) of amorphous phases (fraction of crystalline phases, 1 − f) increases, electrical conductivity decreases, and diffusivity increases. This indicates the possibility of optimizing conduction properties of carbonaceous materials by varying the fraction of each phase [109]. Non-graphitic carbonaceous materials

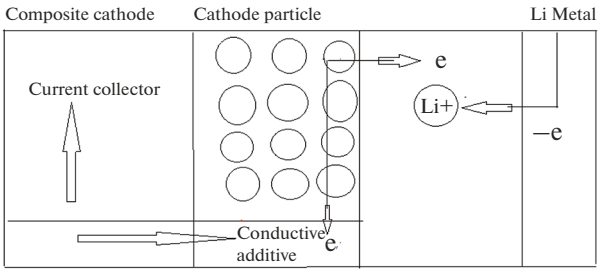

Fig. 3. The conduction phenomena in cathode particle ($LiFePO_4$) during charge.

do not undergo phase transformations and therefore do not show distinctive stages in the OCV curve [110]. The solid electrolyte interphase (SEI) layer displays much lower ionic and electronic conductivity than the bulk electrode. To elucidate the mechanisms related to the properties and performance of Li-ion batteries, precise investigation of the electronic state and the diffusion process in the carbon and the SEI layer is still required. The diffusivity of Li-ions in graphite is complicated by the constant phase change in the Li-graphite intercalation compound (Li-GIC), which can introduce disorder into the originally ordered structure [111]. As the degree of intercalation increases, diffusivity becomes smaller [112]. For this reason, diffusivity is reported as a function of intercalation or electrode voltage [113]. Note that low quality carbon, which has low crystallinity, does not exhibit the staging phenomenon. Carbonaceous materials' properties largely depend on the starting materials (carbon precursor), heat treatment and the final mixture. During discharge, Li^+ ions are extracted from the layered graphite, they pass through the electrolyte and intercalate between the $LiCoO_2$ layers (Figs. 3, 4). The reversible process is:

$$mC + LiCoO_2Li_nC_m + Li_{1-n}CoO_2,$$
$$m \approx 0.5, \quad n = 6, \quad Voc \approx 3.7 \text{ V},$$

where *Voc*—open circuit voltage [87].

In the case of anode, Li metal is found to be the most electropositive (−3.04 V versus standard hydrogen electrode) with large reversible capacity (≈4000 A h kg^{-1}). However, due to safety considerations (explosion hazards as a result of dendrite growth during cycling), metallic Li has been substituted by various carbonaceous materials [114]. Carbon-lithium anodes have much lower gravimetric and volumetric energy densities than pure lithium which lead towards the development of interstitial-free 3d transition metal oxides (M_nO_m, M = Fe, Co, Ni, Mn, Cu). These materials are able to incorporate more than one Li^+ per metal through conversion (displacement) reactions giving higher capacities (≈800 A h kg^{-1}) in comparison to carbon anodes [115–119].

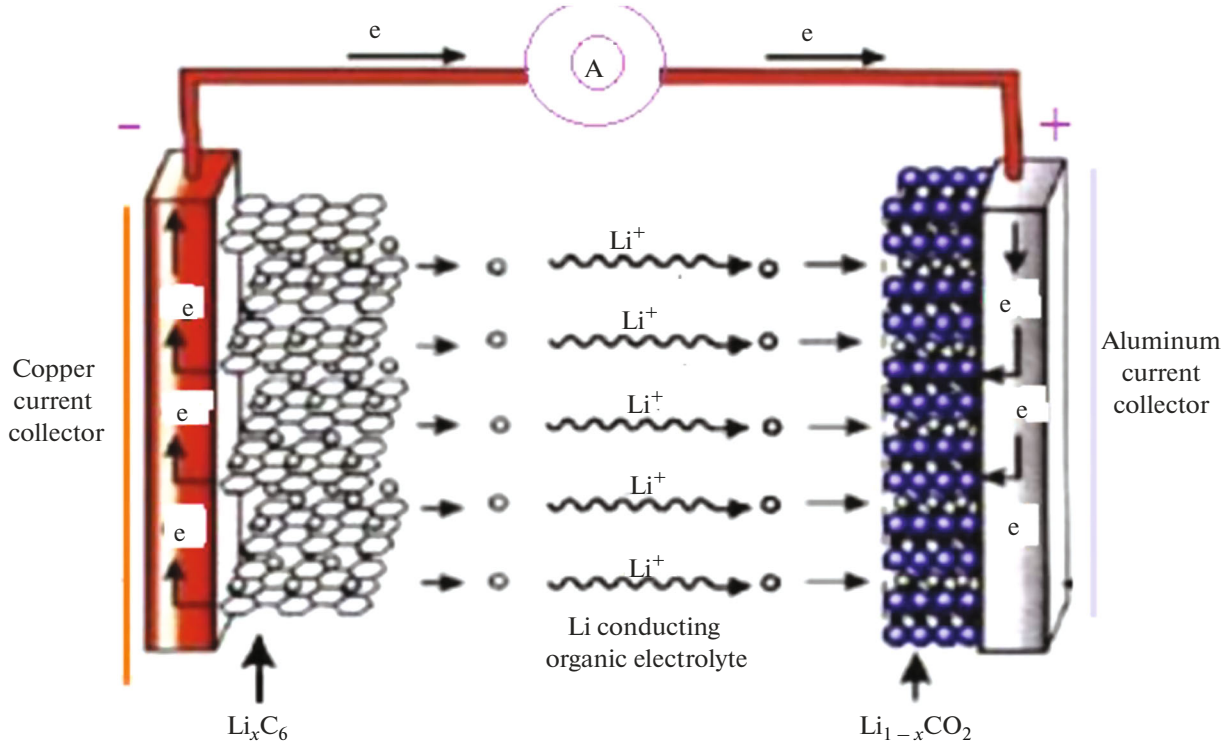

Fig. 4. A typical commercial lithium-ion battery [113].

2.4. Density and Energy of Lithium in Diffusion Model

2.4.1. Electron density profile models. The electron density has been defined as

$$\rho(r) = \eta_i |\varphi_i(r)|^2 = \sum_i \eta_i \left| \sum_l C_{l,i} \chi_i(r) \right|^2, \quad (6)$$

[120–122] where η_i is occupation number of orbital (i), φ is orbital wave function, χ is basis function and C is coefficient matrix, the element of i_{th} row j_{th} column corresponds to the expansion coefficient of orbital j respect to basis function i. Atomic unit for electron density can be explicitly written as e/Bohr^3:

$$\nabla\rho(r) = \left[\left(\frac{\partial\rho(r)}{\partial(x)} \right)^2 + \left(\frac{\partial\rho(r)}{\partial(y)} \right)^2 + \left(\frac{\partial\rho(r)}{\partial(z)} \right)^2 \right]^{\frac{1}{2}}, \quad (7)$$

$$\nabla^2\rho(r) = \frac{\partial^2\rho(r)}{\partial x^2} + \frac{\partial^2\rho(r)}{\partial y^2} + \frac{\partial^2\rho(r)}{\partial z^2} \quad (8)$$

[120–122]. The positive and negative value of this function correspond to electron density is locally depleted and locally concentrated respectively. The relationships between $\nabla^2\rho$ and valence shell electron pair repulsion (VSEPR) model, chemical bond type, electron localization and chemical reactivity have been built by Bader [123].The kinetic energy density is not uniquely defined, since the expected value of kinetic energy operator $\langle\varphi| - \left(\frac{1}{2}\right)\nabla^2\varphi$ can be recovered by integrating kinetic energy density from alternative definitions. One of commonly used definition is:

$$k(r) = -\frac{1}{2}\sum_i \eta_i \varphi_i^*(r) \nabla^2 \varphi_i(r), \quad (9)$$

relative to $K(r)$, the local kinetic energy definition given below guarantee positivizes everywhere; hence the physical meaning is clearer and is more commonly used. The Lagrangian kinetic energy density, "$G(r)$" is also known as positive definite kinetic energy density:

$$G(r) = \frac{1}{2}\sum_i \eta_i |\nabla(\varphi_i|^2$$
$$= \frac{1}{2}\sum_i \eta_i \left\{ \left[\left(\frac{\partial\varphi_i(r)}{\partial(x)} \right)^2 + \left(\frac{\partial\varphi_i(r)}{\partial(y)} \right)^2 + \left(\frac{\partial\varphi_i(r)^2}{\partial(z)} \right) \right] \right\}, \quad (10)$$

where $K(r)$ and $G(r)$ are directly related by Laplacian of electron density

$$\frac{1}{4}\nabla^2\rho(r) = G(r) - K(r). \quad (11)$$

Becke and Edgecombe noted that spherically averaged like spin conditional pair probability has direct correlation with the Fermi hole and then suggested electron localization function (ELF) [124]:

$$\mathrm{ELF}(r) = \frac{1}{1 + \left[D(r)/D_{0(r)} \right]^2}, \quad (12)$$

where

$$D(r) = \frac{1}{2}\sum_i \eta_i |\nabla\varphi_i|^2 - \frac{1}{8}\left[\frac{\|\nabla\rho_\alpha|^2}{\rho_\alpha(r)} + \frac{\|\nabla\rho_\beta|^2}{\beta(r)} \right], \quad (13)$$

and

$$D_{0(r)} = \frac{3}{10}(6\pi^2)^{\frac{2}{3}}\left[\rho_\alpha(r)^{\frac{5}{3}} + \rho_\beta(r)^{\frac{5}{3}} \right], \quad (14)$$

for close-shell system, since

$$\rho_\alpha(r) = \rho_\beta(r) = \frac{1}{2}\rho, \quad (15)$$

D and D_0 terms can be simplified as

$$D(r) = \frac{1}{2}\sum_i \eta_i |\nabla\varphi_i|^2 - \frac{1}{8}\left[\frac{|\nabla\rho|^2}{\rho(r)} \right], \quad (16)$$

$$D_{0(r)} = \frac{3}{10}(3\pi^2)^{\frac{2}{3}}\rho(r)^{\frac{5}{3}}. \quad (17)$$

Savin A. et al. have reinterpreted ELF in the view of kinetic energy [125], which makes ELF also meaningful for Kohn-Sham density functional theory (DFT) wave-function or even post-HF wave-function. They indicated that $D(r)$ reveals the excess kinetic energy density caused by Pauli repulsion, while $D_{0(r)}$ can be considered as Thomas–Fermi kinetic energy density [126]. Localized orbital locator (LOL) is another function for locating high localization regions likewise ELF, defined by Schmider and Becke in the paper [126, 127]

$$\mathrm{LOL}(r) = \frac{\tau(r)}{1 + \tau(r)}, \quad (18)$$

where

$$(r) = \frac{D_0(r)}{\frac{1}{2}\sum_i \eta_i |\nabla\varphi_i|^2}, \quad (19)$$

$D_0(r)$ for spin-polarized system and close-shell system are defined in the same way as in ELF [128].

2.4.2. Local Information Entropy. Local information entropy is a quantification of information, this theory was proposed by Shannon in his study of information transmission in noise channel, and nowadays its application has been largely widened to other areas, including theoretical chemistry. For example, Aslangul and coworkers attempted to decompose diatomic and triatomic molecules into mutually exclusive space by minimizing information entropy [129].

Parr R.G. et al. discussed the relationship between information entropy and atom partition as well as molecular similarity [130]. Noorizadeh and Shakerzadeh suggested using information entropy to study aromaticity [131]. The formula of Shannon's information entropy for normalized and continuous probability function is

$$S = -\int P(x)\ln P(x)\,dx. \quad (20)$$

For chemical system, if $P(x)$ is replaced by $\frac{\rho(r)}{N}$, then the integrand may be called local information entropy of electrons

$$S(r) = -\frac{\rho(r)}{N}\ln\frac{\rho(r)}{N}, \quad (21)$$

where N is the total number of electrons in the current system.

2.4.3. Electrostatic potential. The total electrostatic potential (ESP) measures the electrostatic interaction between a unit point charge placed at r and the system of interest. A positive (negative) value implies that the current position is dominated by nuclear (electronic) charges. Molecular ESP has been widely used for prediction of nucleophilic and electrophilic sites for a long time.

It is also valuable in studying hydrogen bonds, halogen bonds, molecular recognitions, and the intermolecular interaction of aromatics. Moreover, based on statistical analysis, Murray and coworkers found a set of functions called general interaction properties function (GIPF) [132], which connects ESP in molecular surface and macroscopic properties. There are a lot of reviews on ESP, interested readers are suggested to consult [133, 134].

The ESP evaluated under default value is accurate enough in general cases. Reduced density gradient (RDG) and $Sign(\lambda 2)\rho$ are a pair of very important functions for revealing weak interaction region, [135] for detail. The basic applications are exemplified in Sections 4.100.1 and 4.200.1. RDG is defined as

$$\mathrm{RDG}(r) = \frac{1}{2(3\pi^2)^{\frac{1}{3}}}\frac{|\nabla\rho(r)|}{\rho(r)^{\frac{4}{3}}}, \quad (22)$$

by default, x is 0.05, it can be nullify this treatment by setting the parameter to zero,

$$\rho^{\mathrm{pro}}(r) = \sum_A \rho_A^{\mathrm{free,fit}}(r - R_A), \quad (23)$$

where $\rho_A^{\mathrm{free,fit}}$ is pre-fitted spherically averaged electron density of atom A [120–122].

3. COMPUTATIONAL DETAILS

Calculations were performed using both Gaussian and GAMESS-US packages [136]. In this study, we have mainly focused on getting the optimized results for each tube from DFT methods including the m06 and m06-L. The m062x, m06-L, and m06-HF are novel Meta hybrid DFT functional with a good correspondence in non-bonded calculations and are useful for calculating the energies of the distance between two plates of h-BN sheets [137]. Pm6, Extended–Huckel and Pm3MM including pseudo=lanl2 calculations using Gaussian program have done for the non-bonded interaction between two tubs.

M06 and m06-L (DFT) functional is based on an iterative solution of the Kohn-Sham equation [138] of the density functional theory in a plane-wave set with the projector-augmented wave pseudo-potentials. The Perdew–Burke–Ernzerhof (PBE) [139] exchange-correlation (XC) functional of the generalized gradient approximation (GGA) is adopted. The optimizations of the lattice constants and the atomic coordinates are made by the minimization of the total energy. A fixed h-BN sheets geometry with xLi (x = 4–7) is chosen with no further geometry optimization. The outer ring, initially placed at the center of the inner tube, is rigidly axially shifted and rotated around the fixed inner shell. At each inter-tube configuration, a single-point calculation is carried out and the total energy is recorded. The resulting sliding-rotation energy surfaces are used to fix our model in a better position. We employed density functional theory with the van der Waals density functional to model the exchange-correlation energies of h-BN sheets [140]. The double ζ-basis set with polarization orbitals (DZP) were used for x lithium over the h-BN sheets. For non-covalent interactions, the B3LYP method is unable to describe van der Waals [141] capacitor systems by medium-range interactions such as the interactions of two cylinders. The B3LYP and most other functional are correctly insufficient to illustrate the exchange and correlation energy for distant non-bonded medium-range systems. Moreover, some recent studies have shown that inaccuracy for the medium-range exchange energies leads to large systematic errors in the prediction of molecular properties [142, 143]. We further calculated the interaction energy between x lithium an h-BN sheets. The interaction energy was calculated via an Mp6 method in all items according to

$$\Delta E_S\,(\mathrm{eV}) = \{E_{\mathrm{total}} - (E_{x\mathrm{Li}} + E_{h-BN\mathrm{sheets}})\} + E_{\mathrm{BSSE}},$$

where the ΔE_S is the stability energy of system. The charge transfer and electrostatic potential-derived charge were also calculated using the Merz–Kollman–Singh [144], chelp [145], or charges from eLectrostatic potentials using a Grid-based method (chelpG) [146]. The charge calculation methods based on molecular electrostatic potential (MESP) fitting are not well-suited for treating larger systems whereas some of the innermost atoms are located far away from the points at which the MESP is computed. In such a condition, variations of the innermost atomic charges will not lead towards a significant change of the MESP outside of the molecule, meaning that the accurate values for the innermost atomic charges are not well-determined by MESP outside the molecule. This approach (CHELPG) is shown to be considerably less dependent upon molecular orientation than the original CHELP program. The results are compared to those obtained by using CHELP. In the CHELPG (Charges from Electrostatic Potentials

using a Grid based method), atomic charges are fitted to reproduce the molecular electrostatic potential (MESP at a few points around the molecule. The MESP is calculated at a number of grid points spaced 3.0 pm apart and distributed regularly in a cube. Charges derived in this way don't necessarily reproduce the dipole moment of the molecule. CHELPG charges are frequently considered superior to Mulliken charges as they depend much less on the underlying theoretical method used to compute the wave function (and thus the MESP). The representative atomic charges for molecules should be computed as average values over several molecular conformations. The electron density (Both of Gradient norm & Laplacian) have been calculated, value of orbital wave-function, electron spin density, electrostatic potential from nuclear/atomic charges, electron localization function (ELF), localized orbital locator (LOL defined by Becke & Tsirelson), total electrostatic potential (ESP) and the exchange-correlation density, correlation hole and correlation factor, Average local ionization energy using Multifunctional Wave-function Analyzer [120–122].

The contour line map has been drawn via Multiwfn software [120, 121]. The solid lines indicate positive regions, dash lines indicate negative regions. The contour line has drawn corresponding to vdW surface (electron density equals 0.001 a.u., which is defined by Bader R.F.W.). This is useful to analyze distribution of electrostatic potential on vdW surface. Such a contour line has plotted in gradient line and vector field map too by the same option.

The relief map is used to present the height value at every point. If values are too large, they will be truncated in the graph, it can be chosen to scale the data with a factor to avoid truncation. The graph is shown on interactive interface. Shaded surface map and shaded surface map with projection are used in our representation of height value at each situation [120–122]. Before running our experimental work, we focused on several works, first Ivanishcheva et al. [147–149]. In 2022, it was modified the layered oxide of NCM (LiNiCoMnO) with high nickel (Ni) content as a unique strategy for development of energy-dense cathode materials for LIBs. They presented a work with NCM powders were modied by perovskite-like phase La (Li Ni)O(LNP), using lithium residual compounds (LRC) from NCM surface. Initial properties of NCM materials were under their focus in terms of structural data of pristine powders and the capacity loss. They observed that incomplete lithium extraction in the case of LNP-modied NCM bare sample preserves electrochemical performance. Ivanishchev et al. [150] analysed a mechanism of the particles' surface treatment influence on the electrochemical characteristics of the lithium-ion battery cathode active material based on Ni-Rich Layered Oxides with following composition LiNiCoMnO (single-crystal $LiNi_{1-x-y}Co_xMn_yO_2$ (NCM)). They evaluated the result of the practical electrochemical characteristics of the studied NCM samples: the capacity values and their change during repeated charge–discharge cycles were determined. The capabilities of the electrochemical methods such as galvanostatic intermittent titration technique (GITT) and electrochemical impedance spectroscopy (EIS) in their combined application allowed analyzing several charge transfer processes in the material under study, differing in characteristic times. The dependences of the diffusion coefficient of lithium ions in each process on the electrode potential or concentration of lithium ions were confirmed through the analysis of results. Ivanishchev et al. [151] presented a new approach to the determination of electrochemical parameters characterizing the degradation behavior of electrodes based on LiNiCoMnO (Ni-rich NCM) using the method of cyclic voltammetry with a linear scan of the electrode potential (CV). The results of the GITT and EIS were used to verify the CV data. The features of the irreversible phase transition in NCM during the first cycle of extraction-insertion of lithium ions and its influence on the further behavior of the material during cycling were studied. Ivanishcheva I.A. et al. [152] suggested a novel strategy of MAX which is a ternary phase composed of an early transition-metal (M), an A-group element (A) and C, N, B, P (X) phase application in the LIB's cathode composite with high nickel content. Two MAX phase candidates—TSC and TAC (TiSiC and TiAlC, respectively)—with outstanding electronic conductivity were used as LiNiCoMnO-cathode composite (NCM) additive in amount of 1% by weight. They found the optimal post-heat temperature (400°C) to prepare TSC-composite electrode with the enhanced cycling stability its capacity retention was 96 and 89% after 50 cycles at room and elevated temperature of cycling test, respectively. Based on the morphology of MAX phases milled particles with flaky shape, oxidation stability evaluation and electrode resistance measurements

4. EXPERIMENTAL SECTION

Samples from the proposed $LiNi_{1-x}Co_xO_2$ system were synthesized using the sol-gel method [25]. Stoichiometric weight of $LiNO_3$, $Co(Ac)_2{\cdot}2H_2O$ and $Ni(COOCH_3)_2{\cdot}4H_2O$, which were used as precursor agents have been used for fabricant of $Li_xNi_yCo_zO_2$. This synthesis method was mainly used because the chemical reaction is easy, requires only a low reaction temperature and has a high degree of homogeneity compared to the conventional solid-state synthesis. This mixture of precursors was first dissolved in deionized H_2O and then equivalent-molar weights of citric acid were added. This solution was continuously stirred for about 15 min for the formation of a homogeneous mixture of gel and then is kept under in a furnace and is heated to 350°C for 3 h. Finally, the material collected from the furnace is grounded and is

Table 1. Density, energy, Electron localization function (ELF), Localized orbital locator (LOL) and Local Entropy for each Li of 6 lithium diffused on BN and graphene mixed layers

Lithium No.	Density of all electron ($\times10^{-4}$)	Density of *a* electron ($\times10^{-4}$)	Density of β electron ($\times10^{-4}$)	Potential energy density ($\times10^{-3}$J)	Hamiltonian kinetic energy ($\times10^{-4}$J)	LOL ($\times10^{-3}$)	Local entropy ($\times10^{-6}$)	Ellipticity	ELF ($\times10^{-7}$)	Eta index
Li(1)	0.25	0.11	0.11	−0.20	−0.15	0.21	0.45	−0.4	0.4	0.14
Li(2)	0.22	0.14	0.14	−0.25	−0.14	0.21	0.53	−0.15	0.39	0.15
Li(3)	0.24	0.12	0.12	−0.27	−0.15	0.2	0.54	−0.21	0.32	0.16
Li(4)	0.27	0.13	0.13	−0.25	−0.13	0.2	0.52	−0.32	0.36	0.14
Li(5)	0.21	0.11	0.11	−0.26	−0.14	0.22	0.41	−0.32	0.35	0.15
Li(6)	0.23	0.13	0.12	−0.26	−0.14	0.2	0.54	−0.21	0.37	0.15

stored in a dry place until it is made into a cathode. Acetates basically require two heating stages for the formation of a proper phase for end material. The synthesis's temperatures might be selected in order to consideration until all the acetates get decomposed towards a proper phase formation. For the cathode preparation the samples were made by a solid rolling, which is usually used in the lab testing. Besides, 70% active material and 25% of acetylene black were measured and ball milled for 20 minutes, then a polymer binder poly-tetra-fluoro-ethylene (PTFE) was added as the remaining 5% and dried overnight in an oven. The electrodes were punched for forming dimension of 10 × 10 mm and used to fabricate pouch cells. Lithium foil, a polypropylene membrane, and a 1.0 M $LiPF_6$ solution in ethylene carbonate + dimethyl carbonate (EC + DEC; 1 : 2 w/w) were used as the negative electrode, the separator, and the electrode, respectively. The Li-ion transfer characteristics were evaluated using alternating current impedance spectroscopy. Before this measurement, the cells were charged to the desired voltage and relaxed in the open circuit mode for 1 h. All the electrochemical measurements were performed at 25°C. The cross-sectional structures of the $LiCoO_2$ electrodes were investigated using FE-SEM (Hitachi, S-4800, 1.5 kV). The cross-sections were prepared using ion-milling (Hitachi, IM400). The crystalline and surface structures of the $LiCoO_2$ active materials were evaluated using spherical aberration corrected (Cs)-STEM (JEOL, JEM-ARM200F, 200 kV) with energy-dispersive X-ray spectroscopy (EDX) and electron energy loss spectroscopy. For electrochemical testing of the cells an Arbin BT2000 battery testing system is used. These tests were carried out at room temperature and the cells were cycled between 2 and 4.6 V at a C-rate of C/10 through 300 μA constant current. The samples were tested for 5 charge and discharge cycles.

5. RESULTS AND DISCUSSION

5.1. Theoretical Investigation

We have listed the data of density, energy, Electron localization function (ELF), Localized orbital locator (LOL) and Local Entropy, Gap energy, charge from ESP, electrostatic potential, Ionization energy, the Charges of two graphene electrodes and the stability energy of G-(h-$BN)_2$-G and dielectric have been calculated and the related amounts have been plotted in Figs. 5, 6. We have calculated the gradient norm and the Laplacian of electron density via Eqs. (7, 8) for the lithium diffused in the G-h-BN system respectively and the data are listed in Table 1. For calculation the electron spin density from the difference between alpha and beta densities, we have used

$$\rho^s(r) = \rho^\alpha(r) - \rho^\beta(r),$$

then the spin polarization parameter function will be returned instead of spin density

$$\xi(r) = \frac{\rho^\alpha(r) - \rho^\beta(r)}{\rho^\alpha(r) + \rho^\beta(r)}.$$

The absolute value of ξ going from zero to unity corresponds to the local region going from un-polarized case to completely polarized case (Table 1). The kinetic energy density, Lagrangian kinetic energy density, and the electrostatic potential from nuclear/atomic charges can be calculated as Eqs. (9), (10) and

$$V_{\text{nuc}}(r) = \sum_{\text{A}} \frac{Z_{\text{A}}}{|r - R_{\text{A}}|},$$

where R_A and Z_A denote position vector and nuclear charge of atom A, respectively and are listed in Tables 1, 2. If pseudo potential is used, then Z is the number of explicitly expressed electrons. Z can be stand for the atomic charges recorded in the file (the fourth column), at this time V_{nu} is useful for analyzing the differ-

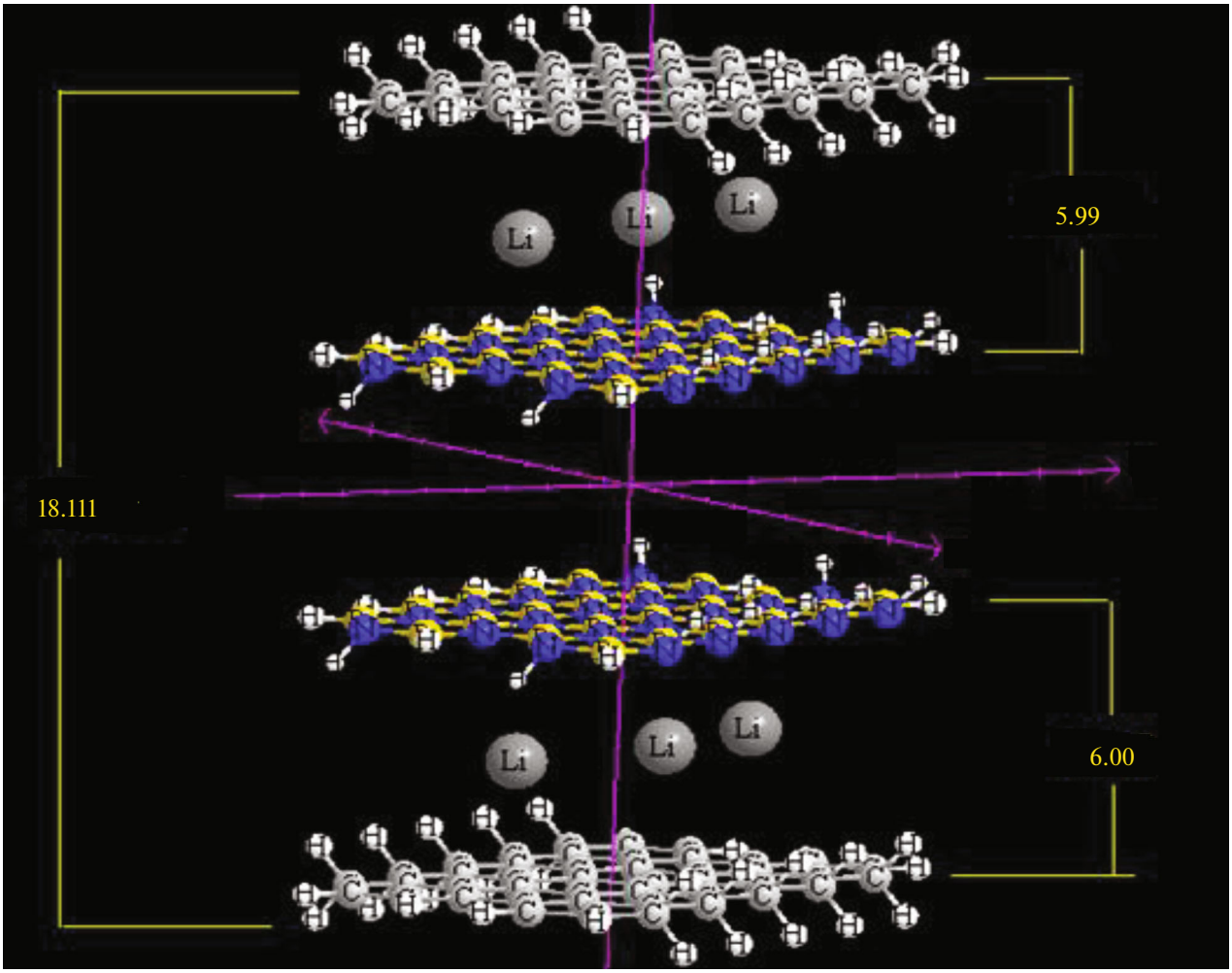

Fig. 5. Six diffused lithium between h-BN and graphene sheet layers.

ence between exact electrostatic potential and the electrostatic potential reproduced by atomic charges. Notice that at nuclear positions, this function will be infinite and may cause some numerical problems in program; hence at these cases this function always returns 1000 instead of infinity. The larger the electron localization is in a region, the more likely the electron motion is confined within it. If electrons are completely localized, then they can be distinguished from the ones outside. Bader found that the regions which have large electron localization must have large magnitudes of Fermi hole integration. However, the Fermi hole is a six-dimension function and thus difficult to be studied visually. Since $D_0(r)$ from Eqs. (11)–(13) is introduced into ELF as reference, what the ELF reveals is a relative localization. ELF is within the range of [0, 1]. A large ELF value means that electrons are greatly localized, indicating that there is a covalent bond, a lone pair or inner shells of the atom involved. In which the actual kinetic energy term in $D(r)$ from Eqs. (15)–(17) is replaced by Kirzhnits type second-order gradient expansion, that is

$$\frac{1}{2}\sum_i \eta_i |\nabla\varphi_i|^2 \approx D_0(r) + \frac{1}{72}\frac{|\nabla\rho|^2}{\rho(r) + \frac{1}{6}\nabla^2\rho(r)},$$

so that ELF is totally independent from wave-function, and then can be used to analyze electron density from X-ray diffraction data (Figs. 7, 8). Of course, Tsirelson's ELF can also be used to analyze electron density from quantum chemistry calculation but is not as good as the ELF defined by Becke owing to the approximation introduced in kinetic energy term; however, qualitative conclusions can still be recovered in general. LOL has a similar expression compared to ELF. In fact, the chemically significant regions that highlighted by LOL and ELF are generally qualitative comparable, while Jacobsen pointed out that LOL conveys more decisive and clearer picture than ELF, Obviously LOL can be interpreted in kinetic energy way as for ELF; however, LOL can also be interpreted

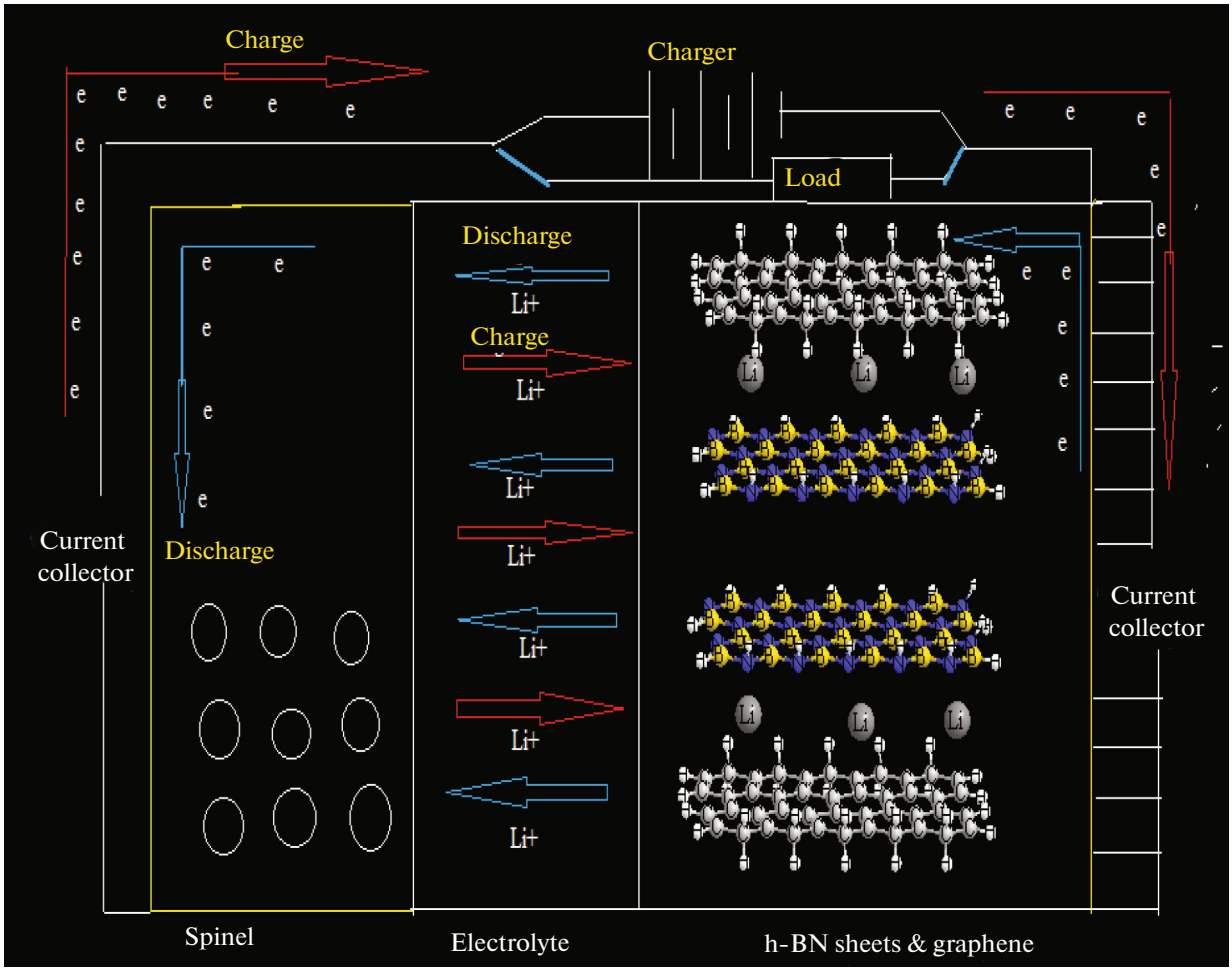

Fig. 6. Operating Li-ion battery.

in view of localized orbital. Small (large) LOL value usually appears in boundary (inner) region of localized orbitals because the gradient of orbital wavefunction is large (small) in this area. The value range of LOL is identical to ELF, namely [0, 1]. In this work, we have calculated the local information entropy for each lithium atom via Eqs. (20)–(21) and the integration of this function over whole space yields information entropy. The data of local information entropy are listed in Tables 1. Weak interaction (Eqs. (21)–(22)) has significant influence on conformation of macromolecules; however, reproduction of electron density by ab initio and grid data calculation of reduced density gradient (RDG) for such huge systems is always too time-consuming (Fig. 9). As lithium has an unpaired electron, leading to a difference in spin-up and spin-down, when two lithium atoms are adsorbed simultaneously electrons get paired and magnet moment disappears.

As a result, spin polarized cluster has a gap which size depends on adsorbed electron–spin polarization. In this work, we have calculated LOL (Fig. 10) and have shown the complex of G-(h-$BN)_2$-G does demonstrate high electrical conductivity, good mechanical strength, excellent flexibility, great chemical stability, and high specific surface area. This is especially noticeable when graphene is chemically converted with a greater proportion of functional groups, proving that it is suited for use as a base composite electrode material. When used as electrode material, G-(h-$BN)_2$-G can effectively reduce the size of the active material, prevent agglomeration of nanoparticles, improve electrons and ions transmission capacity, as well as enhancing the electrode's mechanical stability. As a result (Tables 3, 4), G-(h-$BN)_2$-G-containing electrode materials have high capacity and good rate performance. G-(h-$BN)_2$-G flexibility makes it an ideal material to buffer metal electrode's volume expansion and contraction during the charge–discharge process. Further, the excellent electrical properties of G-(h-$BN)_2$-G can enhance the conductivity of metal electrode material. Smaller particles mean the diffusion distance of lithium ions and electrons is reduced; this improves the material's rate performance. Finally, the lithium storage capacity for

Table 2. Gap energy, charge from ESP, electrostatic potential and Ionization energy for each Li of 6 lithium diffused on BN and graphene mixed layers

Lithium No.	Gap, kJ/mol	Charge from ESP, a.u.	Electrostatic properties, a.u.	Average local ionization energy	Hole for $a \times 10^{-8}$	Laplacian of electron density ($\times 10^{-3}$)
Li(1)	0.05	0.95	–0.14	0.80	–0.12	0.95
Li(2)	0.03	0.95	–0.08	0.83	–0.41	0.14
Li(3)	0.03	0.95	–0.15	0.81	–0.31	0.13
Li(4)	0.04	0.96	–0.12	0.82	–0.22	0.12
Li(5)	0.05	0.96	0.12	0.79	–0.49	0.95
Li(6)	0.06	0.96	0.08	0.79	–0.51	0.14

most metal oxide composite materials with G-(h-$BN)_2$-G can be useful greatly.

5.2. Relationship between Diffusivity and Ionic Conductivity

Although diffusivity is used as a main descriptor for the motion of Li-ions it is indispensable to survey the concept of ionic conduction and the relationship between diffusivity and ionic conductivity because

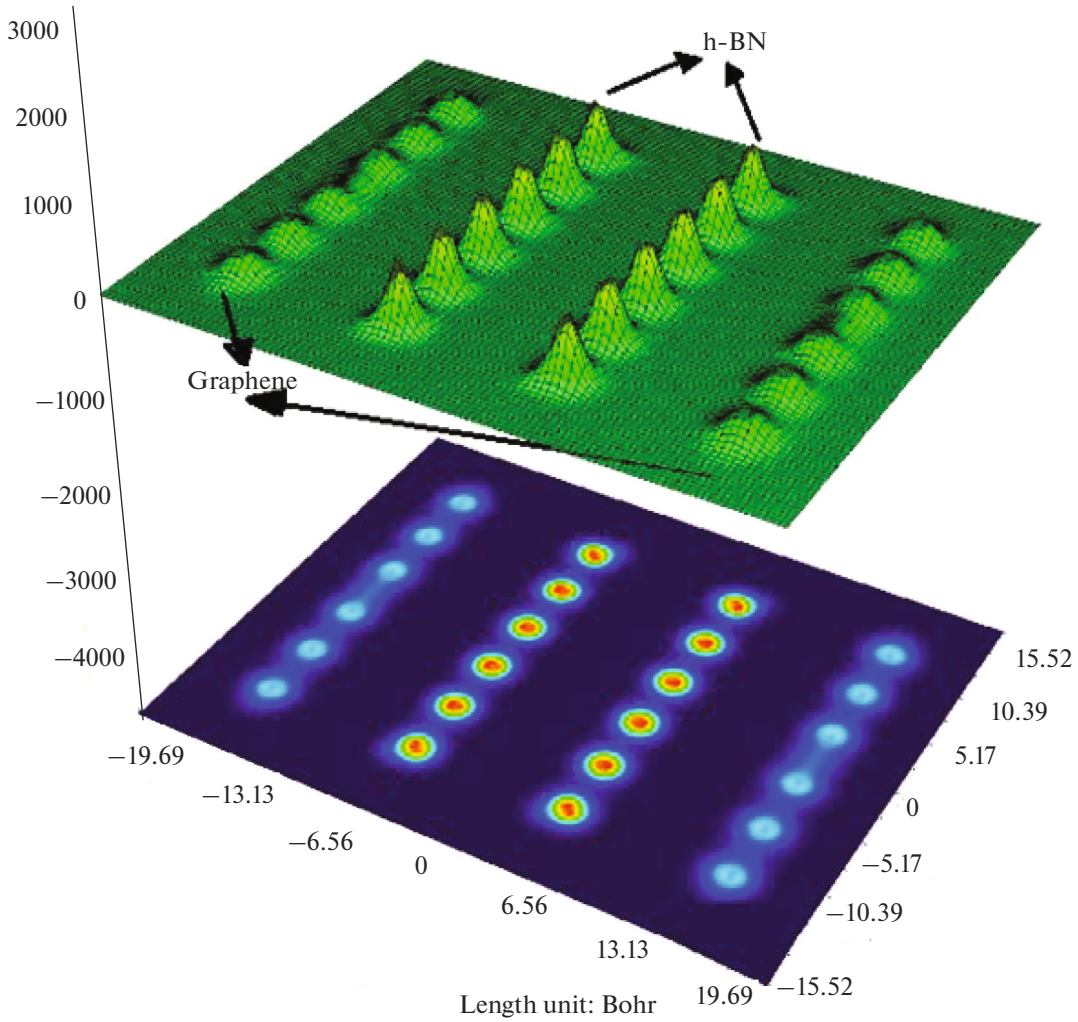

Fig. 7. Density with projection of 6 lithium and h-BN-G systems.

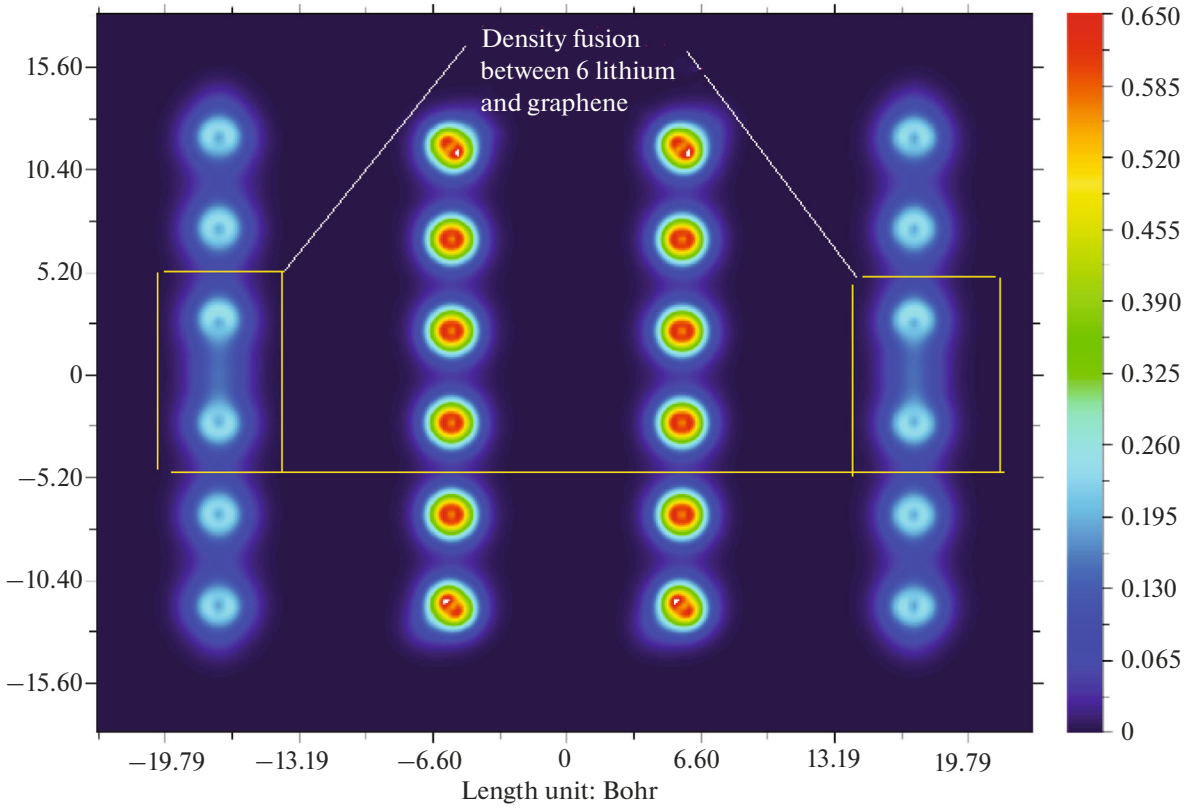

Fig. 8. The density of state lithium and graphene sheets are mixed for h-BN sheets there is no mixing.

ionic conductivity also is important for describing the motion of Li-ions. Motion of a Li-ion gives rise to ionic conduction (i.e. currents) under external electrical potential. In a Li-ion battery, Li-ions should move through the electrolyte from the cathode to the anode during charge, and vice versa during discharge; anything hampering this motion can be interpreted as ionic resistivity. As instance, resistance can originate from inside the electrode materials, from the interface between the electrodes and the electrolyte, and from the electrolyte itself. Charged particles, including Li-ions, can pass through a media under two driving forces: an externally applied electric field or a concentration gradient. The mobility (ui) of ions represents the degree of ease with which ions pass through media when an external electrical field is applied, and the diffusivity (Di) represents the ease with which ions pass through media under a concentration gradient. While

Table 3. The charges of two graphene electrodes and the stability energy of G-(h-BN)$_2$-G

Li_xG-(h-BN)$_2$-G	$\frac{1}{2}$Dielectric thickness, Å	ΔE_S, eV	q^+_{m-G}	q^-_{m-G}
LiG-(h-BN)$_2$-G	5.99	−12.19	+0.34	−0.34
Li_2G-(h-BN)$_2$-G	5.99	−15.65	+0.20	−0.22
Li_3G-(h-BN)$_2$-G	5.98	−22.80	+0.023	−0.07
Li_4G-(h-BN)$_2$-G	5.97	−31.29	+0.007	−0.08
Li_5G-(h-BN)$_2$-G	5.99	−40.12	+0.25	−0.10
Li_6G-(h-BN)$_2$-G	6.03	−43.39	+0.15	−0.020
G-(h-BN)$_2$-G	5.89	−4.78	0.00	0.000

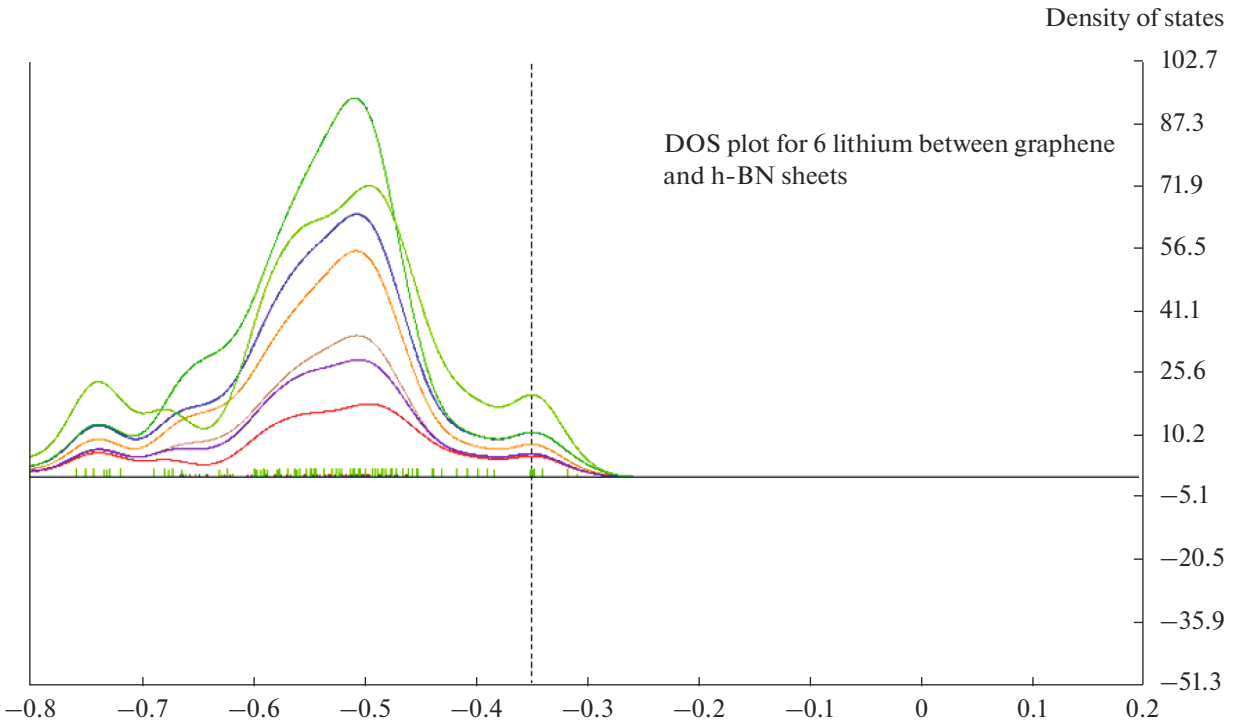

Fig. 9. Density of state plot of "6" lithium has been calculated inside graphene and h-BN sheets.

mobility and diffusivity are often treated as separate phenomena, the key here is that diffusivity, mobility, charges, and ionic conductivity have linear relationship properties with each other.

5.3. Fabrication and Characterization

The data of voltages, charges and discharges are listed in Tables 5, 6 and plotted in Figs. 11–13 for five samples of $LiNi_{1-x}Co_xO_2$ ($x = 1$, 0.8, 0.6, 0.5 and 0.3) of lithium, nickel and cobalt composition with Graphene/(h-BN)$_2$/Graphene(G/h-BN/G) based anodes. It is notable, although the Ni in LIBs gives a high capacity for storing energies; it is also passive and unstable, with a propensity towards destructive reactions with the electrolyte. In fact, the particle feature of this material synthesized by sol-gel method is favorable for the intercalation-de-intercalation reaction of electrodes during the charge-discharge processes, and it is expected to deliver a larger capacity. Moreover, the smaller particle size of both nickel and cobalt in a suitable composition can be improve the electrochemical performance with increasing the ion diffusion pathway during Li^+ intercalation and de-intercalation pro-

Table 4. The dielectric of G/(h-BN)$_2$/G modeled in various Lithium number

Li_xG-(h-BN)$_2$-G	$\frac{1}{2}$Dielectric thickness, Å	$\Delta\left(V_{B-G}^{(1)} - V_{B-G}^{(2)}\right)$, a.u.	k
LiG-(h-BN)$_2$-G	5.99	3.21	2.91
Li_2G-(h-BN)$_2$-G	5.99	3.25	2.62
Li_3G-(h-BN)$_2$-G	5.98	4.13	2.55
Li_4G-(h-BN)$_2$-G	5.97	4.18	2.27
Li_5G-(h-BN)$_2$-G	5.99	5.12	1.17
Li_6G-(h-BN)$_2$-G	6.03	5.71	1.89
G-(h-BN)$_2$-G	5.89	1.23	2.33

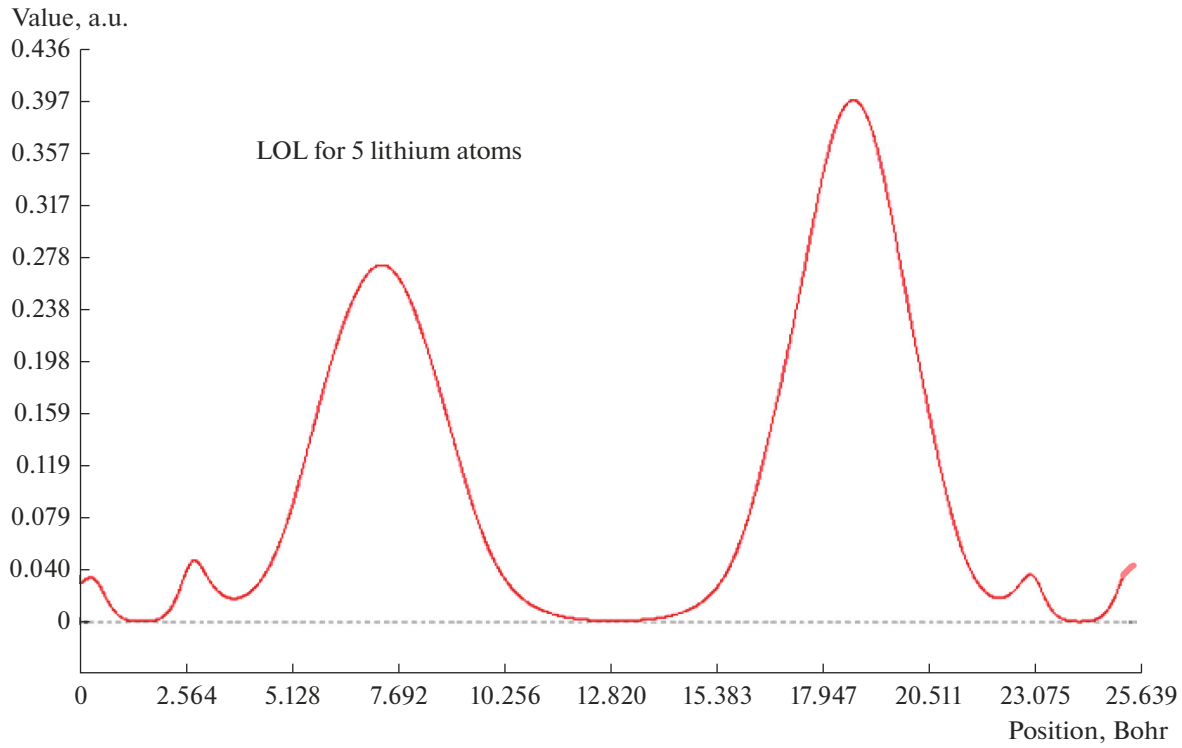

Fig. 10. LOL of 6 and 5 lithium have the same situation and the same plot.

Table 5. Derivative of the capacity and voltage during the charge/discharge process

$\Delta Q/\Delta V$ (mAhg^{-1} V^{-1}) discharge	$\Delta Q/\Delta V$ (mAhg^{-1} V^{-1}) charge	Volte (charge)	Volte (discharge)
0.0	0.0	3.42	3.40
0.0	0.0	3.54	3.53
0.0	0.0	3.61	3.64
0.0	0.0	3.71	3.74
0.0	0.0	3.80	3.83
−2500	0.0	3.92	3.92
−500	3000	3.94	3.93
−200	300	4.02	4.02
−100	200	4.04	4.05
−50	100	4.11	4.10
−100	50	4.16	4.15
−50	50	4.21	4.20
−40	30	4.30	4.30
−100	50	4.40	4.39
−50	100	4.45	4.44
−2000	150	4.50	4.50
−200	500	4.60	4.60
0.0	300	4.68	4.70

Table 6. Correlation between cell volte and diffusivity of $LiNi_{0.2}Co_{0.8}O_2$ (a) and $LiNi_{0.5}Co_{0.5}O_2$ (b)

Charge	Diffusivity	Cell voltage	Charge	Diffusivity	Cell voltage
(a)			(b)		
244.0	8	4.50	245.0	9	4.30
243.5	10	4.47	244.8	12	4.31
243.0	12	4.45	244.4	15	4.32
242.0	14	4.44	244.0	17	4.33
241.0	16	4.44	243.5	19	4.34
240.5	18	4.42	243.0	21	4.35
240.0	20	4.40	242.8	23	4.36
			242.6	25	4.38
			242.4	27	4.39
			242.0	30	4.40

cesses. The initial charge/discharge curves of bare $LiCoO_2$ are curved in Fig. 11. This sample exhibited plateaus due to phase transitions in the high-voltage region of >4.5 V during charge. For evaluating the initial charge/discharge performance, the fabricated cells have been charged to 4.5 V at a constant current density of 0.08, until the current tapered down to 0.01 and the cells were discharged. Their discharge capacities were more than 270 "$mAhg^{-1}$ V^{-1}" which is higher than the theoretical capacity of $LiCoO_2$. Charge-discharge characteristics of $LiNi_{1-x}Co_xO_2$ (x = 1, 0.8, 0.6, 0.5 and 0.3) were investigated by performing cycle tests in the range of 2.0–4.5V in Fig. 12. The initial discharge capacities for $LiNi_{0.7}Co_{0.3}O_2$, $LiNi_{0.4}Co_{0.6}O_2$, $LiNi_{0.2}Co_{0.8}O_2$ and $LiNi_{0.5}Co_{0.5}O_2$ are 183.5, 201.2, 202.5 and 230.5, respectively. It is notable that the irreversible capacity in each point fades because of loss of active materials and could occur either during storage or cycling of the battery. During cycling, there are many factors that could accelerate degradation, such as utilization mode, temperature conditions, etc. Logarithmic irreversible capacities versus cycle number for these kind compositions are much more important for any further discussion. The systems of $LiNi_{1-x}Co_xO_2$, generally possesses high irreversible capacity during the first cycle and higher reversible capacity in subsequent cycles. It is notable that the particle-size of the systems should be in the optimum range so that irreversible capacity is minimum. Although both the reversible capacity and the discharge efficiency are maximum, the useful reversible capacity in these kind systems is low. In fact, the irreversible capacity remains high, and the discharge voltage is substantially higher and gives rise to hysteresis in charge–discharge cycles. The $\Delta Q/\Delta V$ curves (Fig. 13 and Table 5) were calculated from the initial charge/discharge curves. During charge, two peaks that indicate the two-phase were observed in both active materials. These peaks have shifted to the lowest voltage including overlapping each other during the discharge process because of the polarization. The polarization of bare $LiCoO_2$ was larger than that of various $Li_xNi_yCo_zO_2$. Although it is difficult for all the atoms to be recombined in the whole $LiCoO_2$ particle, stacking faults occur and expand in the particle during repeated phase transitions. At the sites the surface of $LiCoO_2$, cells with dissolution of Co cations into the electrolyte are constructed because of the difference in energies between the fault and normal regions. When $LiCoO_2$ is charged at high voltage, most of the Co cations are oxidized. Some of these results have been confirmed theoretically [147] and experimentally [148]. Thus, the result explains how the nickel-substituted phases have good cycling properties with enhanced capacity. The presence of an optimum and suitable mole fraction of nickels instead of cobalt in the lithium site prevents any local collapse of the inter slab space

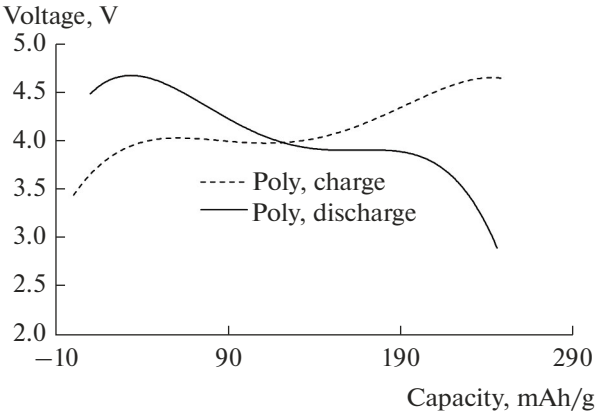

Fig. 11. Charge/discharge curves of bare $LiCoO_2$.

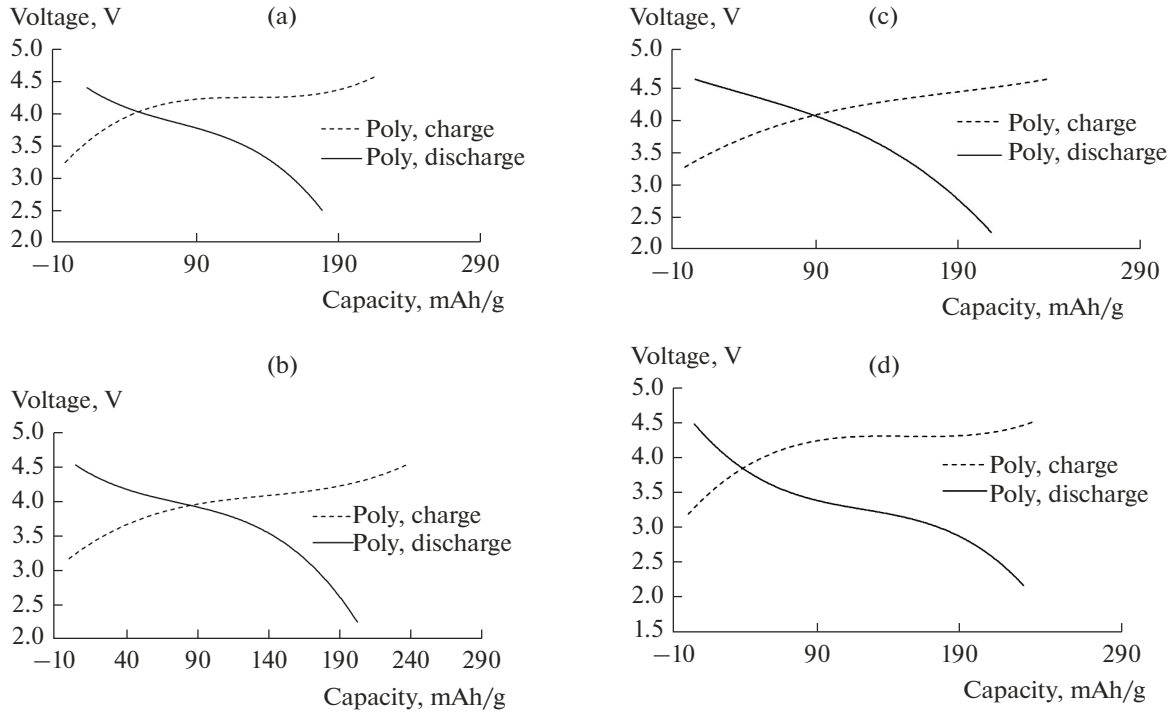

Fig. 12. Charge and discharge curves of $LiNi_{0.7}Co_{0.3}O_2$ (a), $LiNi_{0.4}Co_{0.6}O_2$ (b), $LiNi_{0.2}Co_{0.8}O_2$ (c) and $LiNi_{0.5}Co_{0.5}O_2$ (d).

during the de-intercalation process. At a higher dosage of nickel in the cathode material, the Ni^{2+} preferentially occupies the inter slab spacing during the electrochemical process, which causes the low-capacity delivery. Finally, by this work we exhibited a good performance of composition with fifty/fifty percent of cobalt and nickel in cathode material of lithium ion battery. Derivative of the capacity and voltage during the charge/discharge is calculated, which exhibits the correlation between cell voltage and diffusivity of $LiNi_{0.2}Co_{0.8}O_2$. There is a linear relationship and also a good correlation between diffusivity and charge of $LiNi_{0.5}Co_{0.5}O_2$ in Figs. 14, 15. As it can be confirmed [150], the difference in Li ions diffusion coefficient (D) values in the anodic and cathodic processes, which cor-

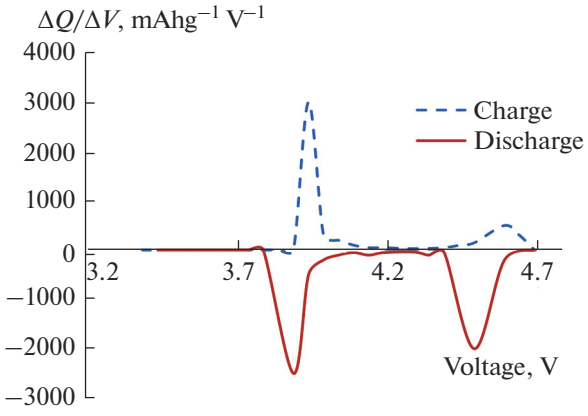

Fig. 13. Derivative of the capacity and voltage during the charge/discharge process.

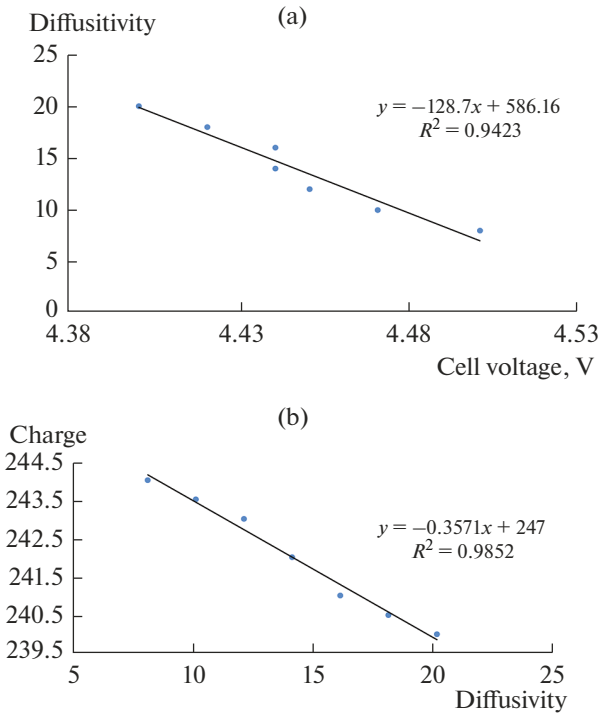

Fig. 14. Correlation between cell volte and diffusivity of $LiNi_{0.2}Co_{0.8}O_2$.

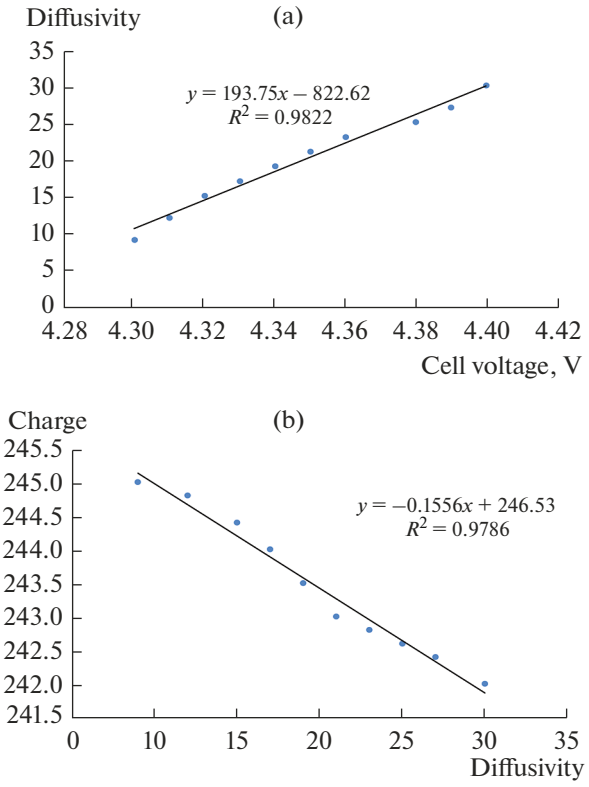

Fig. 15. Correlation between diffusivity and charge of $LiNi_{0.5}Co_{0.5}O_2$.

respond to the current peaks of the cyclic voltammograms in this region, is a criterion for the irreversible degradation of the material's capacity: the greater the difference in the *D* values for these peaks, the higher the irreversible degradation of the material's capacity.

6. CONCLUSIONS

For increasing the capacity, voltage, and amperage for LIBs the composite materials play a strong role. Any theoretical studies in electrode materials (anode and Cathode) of lithium ion batteries and subsequent experimental testing with the results of theory can help us to fabricate powerful batteries with low cost. Using Graphene/$(h\text{-}BN)_2$/Graphene(G/h-BN/G) based anodes with a suitable composite for cathode materials exhibit high voltages and amperages compared with similar condition of the previous LIBs. $LiNi_xCo_{1-x}O_2$ cathodes ($x = 1$, 0.8, 0.6, 0.5 and 0.3) with submicron particles have been successfully synthesized by a sol gel method. The structural and electrochemical properties have been systemically investigated to examine the effects of charge/discharge capacities and capacity retention. The results show that all the prepared $LiNi_xCo_{1-x}O_2$ type layered structure regardless of the nickel content in the range (0.0 up to 0.7) improves the capacity retention significantly. Besides, the Ni promotes the diffusion of Li^+ in $LiNi_xCo_{1-x}O_2$ cathode materials. Moreover, suppresses the phase transitions that usually occur in LiNiO2 during cycling and improves the charge-discharge reversibility of $LiNi_xCo_{1-x}O_2$ systems. The percentage of fifty/fifty nickel and cobalt exhibit a good performance. Although these kind systems can help for removing the disadvantage of cobalt which mainly is its cost and toxic, the performance of these kind systems is similar to $LiCoO_2$ cathode material. Therefore, fabrication of lithium-ion batteries using a few more transition elements such as Mn, Al and Mg is suggested for any further research.

FUNDING

This work was supported by ongoing institutional funding. No additional grants to carry out or direct this particular research were obtained.

CONFLICT OF INTEREST

The authors of this work declare that they have no conflicts of interest.

REFERENCES

1. R. C. Tatar and S. Rabii, Phys. Rev. B **25**, 4126 (1982). https://doi.org/10.1103/PhysRevB.25.4126
2. E. K. Sichel, R. E. Miller, M. S. Abrahams, et al., Phys. Rev. B **13**, 4607–4611 (1976). https://doi.org/10.1103/PhysRevB.13.4607
3. Y.-H. Kim, K. J. Chang, and S. G. Louie, Phys. Rev. B **63**, 205408 (2001). https://doi.org/10.1103/PhysRevB.63.205408
4. A. Zunger, A. Katzir, and A. Halperin, Phys. Rev. B **13**, 5560–5573 (1976). https://doi.org/10.1103/PhysRevB.13.5560
5. W. H. Balmain, J. Prakt. Chem. **27**, 422 (1842). https://doi.org/10.1002/prac.18420270164
6. T. Sato, "Studies on hexagonal and rhomobohedral layered boron nitrides: Synthesis, crystal growth, and transformation under high pressure," *Report of National Institute for Research in Inorganic Materials* (Tsukuba, Japan, 1987).
7. Z.-G. Yang, J.-L. Zhang, M. C. W. Kintner-Meyer, et al., J. Chem. Rev. **111**, 3577–3613 (2011). https://doi.org/10.1021/cr100290v
8. D. Guerard and A. Herold, Carbon **13**, 337–345 (1975). https://doi.org/10.1016/0008-6223(75)90040-8
9. E. J. Yoo, J. Kim, E. Hosono, et al., Nano Lett. **8**, 2277–2282 (2008). https://doi.org/10.1021/nl800957b
10. G. Wang, X. P. Shen, J. Yao, et al., Carbon **47**, 2049–2053 (2009). https://doi.org/10.1016/j.carbon.2009.03.053
11. T. Bhardwaj, A. Antic, B. Pavan, et al., JACS **132**, 12556–12558 (2010). https://doi.org/10.1021/ja106162f

12. T. Suzuki, T. Hasegawa, S. R. Mukai, et al., Carbon **41**, 1933–1939 (2003). https://doi.org/10.1016/S0008-6223(03)00178-7
13. T. Hasegawa, T. Suzuki, S. R. Mukai, et al., Carbon **42**, 2195–2200 (2004). https://doi.org/10.1016/j.carbon.2004.04.045
14. M. Noel and V. Suryanarayanan, J. Power Sources **111**, 193–209 (2002). https://doi.org/10.1016/S0378-7753(02)00308-7
15. J. L. Tirado, Mater. Sci. Eng.: R: Rep. **40**, 103–136 (2003). https://doi.org/10.1016/S0927-796X(02)00125-0
16. L. J. Fu, H. Liu, C. Li, et al., Solid State Sci. **8**, 113–128 (2006). https://doi.org/10.1016/j.solidstatesciences.2005.10.019
17. E. Frackowiak and F. Béguin, Carbon **40**, 1775–1787 (2002). https://doi.org/10.1016/S0008-6223(02)00045-3
18. *Intercalation Chemistry*, Ed. by M. S. Whittingham and A. J. Jacobson (Academic Press, Cambridge, MA, 1982).
19. S. A. Safran and D. R. Hamann, Phys. Rev. Lett. **42** (21), 1410–1413 (1979). https://doi.org/10.1103/PhysRevLett.42.1410
20. M. D. Levi, D. Aurbach, and J. Maier, J. Electroanal. Chem. **624**, 251–261 (2008). https://doi.org/10.1016/j.jelechem.2008.09.014
21. *Graphite Intercalation Compounds I*, Ed. by H. Zabel and S. A. Solin (Springer, Berlin, 1990).
22. Y. P. Wu, E. Rahm, and R. Holze, J. Power Sources **114**, 228–236 (2003). https://doi.org/10.1016/S0378-7753(02)00596-7
23. J. K. Lee, K. W. An, J. B. Ju, et al., Carbon **39**, 1299–1305 (2001). https://doi.org/10.1016/S0008-6223(00)00237-2
24. C. De las Casas and W.-Z. Li, J. Power Sources **208**, 74–85 (2012). https://doi.org/10.1016/j.jpowsour.2012.02.013
25. Z.-H. Yang and H.-Q. Wu, Mater. Chem. Phys. **71**, 7–11 (2001). https://doi.org/10.1016/S0254-0584(00)00512-5
26. K. S. Novoselov, A. K. Geim, S. V. Morozov, et al., Science **306**, 666–669 (2004). https://doi.org/10.1126/science.1102896
27. B. Partoens and F. M. Peeters, Phys. Rev. B **74**, 075404-1–075404-11 (2006). https://doi.org/10.1103/PhysRevB.74.075404
28. H. Tachikawa and A. Shimizu, J. Phys. Chem. B **110**, 20445–20450 (2006). https://doi.org/10.1021/jp061603l
29. K. Naoi, N. Ogihara, Y. Igarashi, et al., J. Electrochem. Soc. **152** (6) (2005) A1047–A1053. https://doi.org/10.1149/1.1896531
30. H. Groult, B. Kaplan, S. Komaba, et al., J. Electrochem. Soc. **150** (2), G67–G75 (2003). https://doi.org/10.1149/1.1531490
31. M. Endo, Y. Nishimura, T. Takahashi, et al., J. Phys. Chem. Solids **57** (6–8), 725–728 (1996). https://doi.org/10.1016/0022-3697(95)00339-8
32. T. Ohzuku and R. J. Brodd, J. Power Sources **174**, 449–456 (2007). https://doi.org/10.1016/j.jpowsour.2007.06.154
33. M. Monajjemi and J. E. Boggs, J. Phys. Chem. A **117**, 1670–1684 (2013). https://doi.org/10.1021/jp312073q
34. M. Monajjemi, V. S. Lee, M. Khaleghian, et al., J. Phys. Chem. C **114**, 15315 (2010). https://doi.org/10.1021/jp104274z
35. M. Monajjemi, J. Mol. Model. **20**, 2507 (2014). https://doi.org/10.1007/s00894-014-2507-y
36. M. Monajjemi, M. Khaleghian, N. Tadayonpour, et al., Int. J. Nanosci. **09**, 517–529 (2010). https://doi.org/10.1142/S0219581X10007071
37. M. Monajjemi, Struct. Chem. **23**, 551–580 (2012). https://doi.org/10.1007/s11224-011-9895-8
38. F. Mollaamin, A. Ilkhani, N. Sakhaei, et al., J. Comput. Theor. Nanosci. **12**, 3148–3154 (2015). https://doi.org/10.1166/jctn.2015.4092
39. M. Monajjemi, Chem. Phys. **425**, 29–45 (2013). https://doi.org/10.1016/j.chemphys.2013.07.014
40. F. Mollaamin and M. Monajjemi, J. Mol. Model. **29**, 119 (2023). https://doi.org/10.1007/s00894-023-05526-3
41. G. V. Simbirtseva and S. D. Babenko, Russ. J. Phys. Chem. B **17**, 1309–1310 (2023). https://doi.org/10.1134/S1990793123060222
42. M. Monajjemi and F. Mollaamin, J. Clust. Sci. **23**, 259–272 (2012). https://doi.org/10.1007/s10876-011-0426-y
43. L. Ravagnan, P. Piseri, M. Bruzzi, et al., Phys. Rev. Lett. **98**, 216103 (2007). https://doi.org/10.1103/PhysRevLett.98.216103
44. P. N. Vishwakarma and S. V. Subramanyam, J. Appl. Phys. **100**, 113702 (2006). https://doi.org/10.1063/1.2372585
45. G. Rizzoni, *Principles and Applications of Electrical Engineering*, 4th ed. (McGraw Hill, New York, 2004), pp. 43–44.
46. K. Kitoh and H. Nemoto, J. Power Sources **81–82**, 887–890 (1999). https://doi.org/10.1016/S0378-7753(99)00125-1
47. H. Maleki, S. A. Hallaj, J. R. Selman, et al., J. Electrochem. Soc. **146** (3), 947–954 (1999). https://doi.org/10.1149/1.1391704
48. J. M. Tarascon and M. Armand, Nature **414**, 359 (2001). https://doi.org/10.1038/35104644
49. A. S. Claye, J. E. Fischer, C. B. Huffman, et al., J. Electrochem. Soc. **147**, 2845 (2000). https://doi.org/10.1149/1.1393615
50. J. N. Barisci, G. C. Wallace, and R. H. Baughman, Electrochim. Acta **46**, 509 (2000). https://doi.org/10.1016/S0022-0728(00)00179-0
51. J. Zhao, A. Buldum, J. Han, et al., Phys. Rev. Lett. **85**, 1706 (2000). https://doi.org/10.1103/PhysRevLett.85.1706
52. F. Mollaamin, S. Mohammadi, Z. Khalaj, et al., Russ. J. Phys. Chem. B **18** (1), 67–82 (2024). https://doi.org/10.1134/S1990793124010330

53. M. A. A. Zadeh, H. Lari, L. Kharghanian, et al., J. Comput. Theor. Nanosci. **12**, 4358 (2015). https://doi.org/10.1166/jctn.2015.4366
54. K. Bakhshi, F. Mollaamin, and M. Monajjemi, J. Comput. Theor. Nanosci. **8**, 763–768 (2011). https://doi.org/10.1166/jctn.2011.1750
55. F. Mollaamin and M. Monajjemi, Russ. J. Phys. Chem. B **18** (2), 533–548 (2024). https://doi.org/10.1134/S199079312402012X
56. M. Monajjemi, M. T. Baie, and F. Mollaamin, Russ. Chem. Bull. **59**, 886–889 (2010). https://doi.org/10.1007/s11172-010-0181-5
57. G. T. Wu, C. S. Wang, X. B. Zhang, et al., J. Power Sources **75**, 175–179 (1998). https://doi.org/10.1016/S0378-7753(98)00106-2
58. H. Jalilian and M. Monajjemi, Jpn. J. Appl. Phys. **54**, 085101 (2015). https://doi.org/10.7567/JJAP.54.085101
59. M. Monajjemi, Theor. Chem. Acc. **134**, 77 (2015). https://doi.org/10.1007/s00214-015-1668-9
60. E. Frackowiak, S. Gautier, H. Gaucher, et al., Carbon **37**, 61–69 (1999). https://doi.org/10.1016/S0008-6223(98)00187-0
61. F. Mollaamin and M. Monajjemi, Russ. J. Phys. Chem. B **18** (2), 607–623 (2024). https://doi.org/10.1134/S1990793124020271
62. B. Gao, C. Bower, J. D. Lorentzen, et al., Chem. Phys. Lett. **327**, 69 (2000). https://doi.org/10.1016/S0009-2614(00)00851-4
63. M. Monajjemi, H. Baheri, and F. Mollaamin, J. Struct. Chem. **52**, 54–59 (2011). https://doi.org/10.1134/S0022476611010070
64. H. Shimoda, B. Gao, X. P. Tang, et al., Phys. Rev. Lett. **88**, 015502 (2002). https://doi.org/10.1103/PhysRevLett.88.015502
65. F. Mollaamin and M. Monajjemi, Russ. J. Phys. Chem. B **18** (1), 49–66 (2024). https://doi.org/10.1134/S1990793124010159
66. M. Monajjemi, R. Wayne Jr., and J. E. Boggs, Chem. Phys. **433**, 1–11 (2014). https://doi.org/10.1016/j.chemphys.2014.01.017
67. M. Monajjemi, H. Yamola, and F. Mollaamin, Fuller. Nanotub. Carbon Nanostruct. **22**, 595–603 (2014). https://doi.org/10.1080/1536383X.2012.702163
68. S. Y. Chew, S. H. Ng, J. Wang, et al., Carbon **47**, 2976–2983 (2009). https://doi.org/10.1016/j.carbon.2009.06.045
69. M. Monajjemi, M. Falahati, and F. Mollaamin, Ionics **19**, 155–164 (2013). https://doi.org/10.1007/s11581-012-0708-x
70. A. Tahan, F. Mollaamin, and M. Monajjemi, Russ. J. Phys. Chem. A **83**, 587–597 (2009). https://doi.org/10.1134/S003602440904013X
71. S. Shahriari, F. Mollaamin, and M. Monajjemi, Micromachines **14**, 241 (2023). https://doi.org/10.3390/mi14020241
72. M. Monajjemi, S. Mohammadi, S. Shahriari, et al., Russ. J. Phys. Chem. B **18**, 308–324 (2024). https://doi.org/10.1134/S1990793124010342
73. M. Monajjemi, L. Mahdavian, F. Mollaamin, et al., Russ. J. Inorg. Chem. **54**, 1465–1473 (2009). https://doi.org/10.1134/S0036023609090216
74. J. Zhao, Q.Y. Gao, C. Gu, et al., Chem. Phys. Lett. **358**, 77 (2002). https://doi.org/10.1016/S0009-2614(02)00580-8
75. H. Zhang, G. Cao, Z. Wang, et al., Electrochim. Acta **55**, 2873–2877 (2010). https://doi.org/10.1016/j.electacta.2010.01.028
76. G. Che, B. Lakshmi, E. Fisher, et al., Nature **393**, 346–349 (1998). https://doi.org/10.1038/30694
77. M. Khaleghian, M. Zahmatkesh, F. Mollaamin, et al., Fuller. Nanotub. Carbon Nanostruct. **19**, 251–261 (2011). https://doi.org/10.1080/15363831003721757
78. N. A. Kaskhedikar and J. Maier, Adv. Mater. **21**, 2664–2680 (2009). https://doi.org/10.1002/adma.200901079
79. A. Thess, R. Lee, P. Nikolaev, et al., Science **273**, 483–487 (1996). https://doi.org/10.1126/science.273.5274.483
80. Y. Ando, X. Zhao, H. Shimoyama, et al., Int. J. Inorg. Mater. **1**, 77–82 (1999). https://doi.org/10.1016/S1463-0176(99)00012-5
81. M. F. Yu, O. Lourie, M. J. Dyer, et al., Science **287**, 637–640 (2000). https://doi.org/10.1126/science.287.5453.637
82. L. F. Cui, L. Hu, J. W. Choi, et al., ACS Nano **4**, 3671–3678 (2010). https://doi.org/10.1021/nn100619m
83. Q. Wang and J. H. Li, J. Phys. Chem. C **111**, 1675–1682 (2007). https://doi.org/10.1021/jp066655p
84. S. H. Ng, J. Wang, Z. P. Guo, et al., Electrochim. Acta **51**, 23–28 (2005). https://doi.org/10.1016/j.electacta.2005.04.045
85. A. Kiebele and G. Gruner, Appl. Phys. Lett. **91**, 144104 (2007). https://doi.org/10.1063/1.2795328
86. X. Chen, C.-Y. Liu, T.-H. Jen, et al., Chem. Mater. **19** (21), 5194–5199 (2007).
87. W. Wang, R. Epur, and P. N. Kumta, Electrochem. Commun. **13**, 429–432 (2011). https://doi.org/10.1016/j.elecom.2011.02.012
88. C. De las Casas and W.-Z. Li, J. Power Sources **208**, 74–85 (2012). https://doi.org/10.1016/j.jpowsour.2012.02.013
89. R. R. Kayumov, A. P. Radaeva, A. A. Krupina, et al., Russ. J. Phys. Chem. B **17**, 801–809 (2023). https://doi.org/10.1134/S1990793123040097
90. M. Senami, Y. Lkeda, A. Fukushima, et al., AIP Adv. **1**, 042106 (2011). https://doi.org/10.1063/1.3651182
91. A. Rubio, J. L. Corkill, and M. L. Cohen, Phys. Rev. B **49**, 1952 (1994). https://doi.org/10.1103/PhysRevB.49.1952
92. N. G. Chopra, R. J. Luyken, and K. Cherrey, Science **269**, 966–967 (1995). https://doi.org/10.1126/science.269.5226.966

93. L. Sun, S. Xie, W. Liu, et al., Nature **403**, 384 (2000). https://doi.org/10.1038/35000290
94. X. Zhao, Y. Liu, S. Inoue, et al., Phys. Rev. Lett. **92**, 125502 (2004). https://doi.org/10.1103/PhysRevLett.92.125502
95. S. Okada, S. Saito, and A. Oshiyama, Phys. Rev. B **65**, 165410 (2002). https://doi.org/10.1103/PhysRevB.65.165410
96. D. S. Wilkinson, *Mass Transport in Solid and Fluids* (Cambridge Univ. Press, Cambridge, UK, 2000).
97. H. Mehrer, *Diffusion in Solids* (Springer, Berlin, 2007), pp. 27–36.
98. D. A. Porter and K. E. Easterling, *Phase Transformations in Metals and Alloys*, 2nd ed. (Chapman and Hall, London, 1992), pp. 1–109.
99. R. H. Petrucci and W. S. Harwood, *General Chemistry*, 7th ed. (Prentice-Hall, Hoboken, NJ, 1997), pp. 315–343.
100. H. Dehmelt, Phys. Scr. **T22** (1988) 102–110. https://doi.org/10.1088/0031-8949/1988/T22/016
101. J. Molenda, Polish J. Chem. **78**, 1413–1421 (2004).
102. S. N. Li, S. H. Luo, L. Yang, et al., Rare Met. **40**, 3477–3484 (2021). https://doi.org/10.1007/s12598-021-01783-4
103. R. A. Huggins, in *Proc. NATO Adv. Study Inst. Solid State Batteries, Alcabideche, Portugal*, Ed. by C. A. C. Sequeira and A. Hooper (1984).
104. F. Mollaamin and M. Monajjemi, Int. J. Quantum Chem. **124**, e27348 (2024). https://doi.org/10.1002/qua.27348
105. J. Cabana, L. Monconduit, D. Larcher, et al., Adv. Mater. **22** (35), E170–E192 (2010). https://doi.org/10.1002/adma.201000717
106. P. Poizot, S. Laruelle, S. Grugeon, et al., Nature **407** (6803), 496–499 (2000). https://doi.org/10.1038/35035045
107. J. C. Park, J. Kim, H. Kwon, et al., Adv. Mater. **21** (7), 803–807 (2009). https://doi.org/10.1002/adma.200800596
108. C. M. Ban, Z. C. Wu, D. T. Gillaspie, et al., Adv. Mater. **22** (20), E145–E149 (2010). https://doi.org/10.1002/adma.200904285
109. A. V. Churikov, N. A. Gridina, and N. V. Churikova, in *New Carbon Based Materials for Electrochemical Energy Storage Systems*, Ed. by I. V. Barsukov, C. S. Johnson, J. E. Doninger, and V. Z. Barsukov (Springer, Dordrecht, 2006), pp. 269–276.
110. J. Dahn and G. M. Ehrlich, Lithium ion batteries, in *Linden's Handbook of Batteries*, 4th ed., Ed. by T. B. Reddy (McGraw Hill, New York, 2011), Ch. 26.
111. A. Funabiki, M. Inaba, Z. Ogumi, et al., J. Electrochem. Soc. **145** (1), 172–178 (1998). https://doi.org/10.1149/1.1838231
112. Y. N. Li, J. Yang, and Z. Jiang, J. Phys. Chem. Solids **67**, 882–886 (2006). https://doi.org/10.1016/j.jpcs.2005.11.003
113. B. Scrosati and J. Garche, J. Power Sources **195** (9), 2419–2430 (2010). https://doi.org/10.1016/j.jpowsour.2009.11.048
114. F. Cheng, J. Liang, Z. Tao, et al., Adv. Mater. **23** (15), 1695–1715 (2011). https://doi.org/10.1002/adma.201003587
115. S. G. Fedorenko, Russ. J. Phys. Chem. B **18**, 210–219 (2024). https://doi.org/10.1134/S1990793124010251
116. M. Monajjemi, R. Faham and F. Mollaamin, Fuller. Nanotub. Carbon Nanostruct. **20**, 163–169 (2012). https://doi.org/10.1080/1536383X.2010.533310
117. S. Link, C. Neef, and T. Wicke, Batteries **9**, 261 (2023). https://doi.org/10.3390/batteries9050261
118. T. Yang, C.-T. Chin, C.-H. Cheng, et al., Nanomaterials **13**, 628 (2023). https://doi.org/10.3390/nano13040628
119. M. E. Sigl, S. Grabmann, L.-F. Kick, et al., Batteries **8**, 174 (2022). https://doi.org/10.3390/batteries8100174
120. T. Lu and F. Chen, Acta Chim. Sinica **69**, 2393–2406 (2011).
121. T. Lu and F. Chen, J. Mol. Graph. Model. **38**, 314–323 (2012). https://doi.org/10.1016/j.jmgm.2012.07.004
122. T. Lu and F. Chen, "Multiwfn: A multifunctional wavefunction analyzer," J. Comp. Chem. 33, 580–592 (2012). https://doi.org/10.1002/jcc.22885
123. R. F. W. Bader, *Atoms in Molecule: A Quantum Theory* (Oxford Univ. Press, Oxford, 1990).
124. A. Becke and K. Edgecombe J. Chem. Phys. **92**, 5397–5403. https://doi.org/10.1063/1.458517
125. A. Savin, R. Nesper, S. Wengert, et al., Angew. Chem. Int. Ed. Engl. **36**, 1808–1832 (1997). https://doi.org/10.1002/anie.199718081
126. V. Tsirelson and A. Stash, Chem. Phys. Lett. **351**, 142–148 (2002). https://doi.org/10.1016/S0009-2614(01)01361-6
127. H. L. Schmider and A. D. Becke, J. Mol. Struct. (THEOCHEM) **527**, 51–61 (2000). https://doi.org/10.1016/S0166-1280(00)00477-2
128. H. Jacobsen, Can. J. Chem. **86**, 695 (2008). https://doi.org/10.1139/v08-052
129. C. Aslangul, R. Constanciel, R. Daudel, et al., Adv. Quantum Chem. **6**, 93–141 (1972). https://doi.org/10.1016/S0065-3276(08)60542-0
130. R. G. Parr, P. W. Ayers, and R. F. Nalewajski, J. Phys. Chem. A **109** (17), 3957–3959 (2005). https://doi.org/10.1021/jp0404596
131. S. Noorizadeh and E. Shakerzadeh, Phys. Chem. Chem. Phys. **12**, 4742–4749 (2010). https://doi.org/10.1039/B916509F
132. J. S. Murray, T. Brinck, P. Lane, et al., J. Mol. Struct.: THEOCHEM **307**, 55–64 (1994). https://doi.org/10.1016/0166-1280(94)80117-7
133. J. S. Murray and P. Politzer, WIRES Comput. Mol. Sci. **1**, 153–163 (2011). https://doi.org/10.1002/wcms.19
134. P. Politzer and J. Murray, Theor. Chem. Acc. **108**, 134–142 (2002). https://doi.org/10.1007/s00214-002-0363-9

135. R. Bonaccorsi, E. Scrocco, and J. Tomasi, J. Am. Chem. Soc. **98** (14), 4049–4054 (1976). https://doi.org/10.1021/ja00430a005
136. M. W. Schmidt, K. K. Baldridge, J. A. Boatz, et al., J. Comp. Chem. **14** (11), 1347–1363 (2004). https://doi.org/10.1002/jcc.540141112
137. Y. Zhao and D.G. Truhlar, Theor. Chem. Account. **120**, 215–241 (2008). https://doi.org/10.1007/s00214-007-0310-x
138. W. Kohn and L. J. Sham, Phys. Rev. **140**, A1133 (1965). https://doi.org/10.1103/PhysRev.140.A1133
139. J. P. Perdew, K. Burke, M. Ernzerhof, Phys. Rev. Lett. **77**, 3865–3868 (1996). https://doi.org/10.1103/PhysRevLett.77.3865
140. D. Klein, R. Roth, A. Lim, et al., Nature **389**, 699–701 (1997). https://doi.org/10.1038/39535
141. Y. Zhao and D. G. Truhlar, Acc. Chem. Res. **41** (2), 157–167 (2008). https://doi.org/10.1021/ar700111a
142. C. E. Check and T. M. Gilbert, J. Org. Chem. **70**, 9828–9834 (2005). https://doi.org/10.1021/jo051545k
143. S. Grimme, Angew. Chem., Int. Ed. **45**, 4460–4464 (2006). https://doi.org/10.1002/anie.200600448
144. B. H. Besler, K. M. Merz, and P. A. Kollman, J. Comp. Chem. **11**, 431–439 (1990). https://doi.org/10.1002/jcc.540110404
145. L. E. Chirlian and M. M. Francl, J. Comp. Chem. **8**, 894–905 (1987). https://doi.org/10.1002/jcc.540080616
146. C. M. Breneman and K. B. Wiberg, J. Comp. Chem. **11**, 361–373 (1990). https://doi.org/10.1002/jcc.540110311
147. M. D. Chien, M. T. D. Dung, and M. Monajjemi, J. Comp. Theor. Nanosci. **14**, 2368–2382 (2017). https://doi.org/10.1166/jctn.2017.6835
148. H. Liu, Y.P. Wu, E. Rahm, et al., J. Solid State Electrochem. **8**, 450–466 (2004). https://doi.org/10.1007/s10008-004-0521-1
149. I. A. Ivanishcheva, A. V. Ivanishchev, J. H. Chang, et al., Batteries and Supercaps **6** (3), e202200466 (2023). https://doi.org/10.1002/batt.202200466
150. A. V. Ivanishchev, S.-H. Lee, J.-J. Kim, et al., J. Electroanal. Chem. **932**, 117242 (2023). https://doi.org/10.1016/j.jelechem.2023.117242
151. A. V. Ivanishchev, I. A. Ivanishcheva, S. Lee, et al., J. Electroanal. Chem. **950**, 117864 (2023). https://doi.org/10.1016/j.jelechem.2023.117864
152. I. A. Ivanishcheva, A. V. Ivanishchev, J.-J. Kim, et al., J. Energy Storage **74**, 109379 (2023). https://doi.org/10.1016/j.est.2023.109379